Petrophysical characterization, microfacies analysis, and diagenetic attributes of the Lower Jurassic surface analog sequence in Gebel El-Maghara area, north Sinai, Egypt

Bassem Nabawy (bsnabawy@yahoo.co.uk)
National Research Centre https://orcid.org/0000-0003-4391-7540
Abdelbaset M. Abudeif
Sohag University Faculty of Science
Marwa M. Masoud
Sohag University Faculty of Science

Research Article

Keywords: Microfacies, petrophysics, RQI, HFU, Lower Jurassic, Gebel EL-Maghara

Posted Date: March 10th, 2021

DOI: https://doi.org/10.21203/rs.3.rs-163788/v1

Abstract

This study concerns with the petrophysical characteristics of the Lower Jurassic surface analog in Gebel El-Maghara area (from base to top Mashaba, Rajabia, and Shusha formations), north Sinai, Egypt and implementation of the mineral components and diagenetic controls on reservoir characteristics. A full set of petrophysical measurements including porosity ($\emptyset_{He}$), permeability (k), grain and bulk densities (σ_g and σ_b, respectively), and true formation resistivity factor was applied. The Lower Jurassic sequence is subdivided into five hydraulic flow units (HFUs) that consist of three reservoir rock types (RRTs). These RRTs are composed of three microfacies association (MFAs). The RRT1 plug samples consist of the mostly clastic MFA1; they are porous, permeable, and have good reservoir quality that is using the flow zone indicator (FZI), and the reservoir quality index (RQI). The lowest reservoir quality is assigned to the RRT samples which are mostly composed tight carbonates.

Based on the petrographical studies, SEM imaging, and the XRD analysis, dissolution and fracturing slightly enhanced the reservoir potentiality of the RRT1 samples, whereas physical compaction, tight cementation, and authigenic clay content (kaolinite, hematite, and goethite) are responsible for deterioration of the reservoir properties of RRT3 samples and reduction of the RRT2 samples.

1. Introduction

Gebel El Maghara massif is a NE-SW elongated asymmetrical double plunged anticline fold extends for 54 km length, and 30 km width. It is the highest and widest topography (of 1300 km^2 as a total area) in the northern parts of Sinai and Egypt; it is located between Lat. 30°35' & 30°50' N, and Long. 33°10' & 33°35' E (Fig. 1). It is the type section of the Jurassic sequence in Sinai Peninsula and represents the thickest Jurassic exposure in Egypt. The Jurassic sediments represent the core of Gebel El-Maghara massif, whereas the Cretaceous and Eocene sediments are represented along its flanks. The area is one of the most important Jurassic exposures in Egypt which are of limited number and mostly situated in north Sinai as surface massive exposures.

It has been studied geologically and palaeontologically studied by many authors (e.g., Farag, 1959; Kostandi, 1959; Al-Far, 1966; Jenkins, 1982, 1990; El Manawi, 1986; Yussef, 1986; Moustafa and Khalil, 1990; Kassab et al., 2016, 2017; Nabawy and Abd El Aal, 2019a). Though the limited Jurassic deposits in Egypt, it is a prospective for hydrocarbon accumulations in some subsurface equivalents in the Western Desert and the Gulf of Suez.

Therefore, this study aims at characterization of the petrophysical properties of the Lower Jurassic analogs at Gebel El-Maghara area and to check their potentiality as hydrocarbon and water-bearing sequence. This could be achieved by studying their storage and flow capacities, and reservoir quality. Rock typing and dividing the sequence into some flow units were also achieved by estimating the reservoir quality parameters of Amaefule et al. (1993) including the flow zone indicator (FZI), and the reservoir quality index (RQI). Besides revealing the mineral components of the studied sequence and the controlling diagenetic factors were also studied.

2. Geologic And Structural Setting

Gebel El-Maghara area is covered mainly by Jurassic and Cretaceous rock sequences. It is the type section of the Jurassic rock sequence in Sinai with the highest thickness (1898 m), and it is the most complete Jurassic outcrops in Egypt. They range in age from the Hettangian to Kimmeridgian age. This Hettangian-Kimmeridgian sequence was classified into six intercalated continental and marine formations, from base to top they are: Mashaba, Rajabia, Shusha, Bir El-Maghara, Safa and Masajid formations. It represents three cycles of intercalated sea regressions and transgressions (Al-Far 1966; Jenkins et al. 1982; Abd El Aal & Lelek 1994).

The present study concerns with the Lower Jurassic Mashaba, Rajabia, and Shusha formations. Mashaba Formation was deposited in fluvial to paralic environment at its base followed by a low energy marine transgression. Upwards, the predominant environments of Rajabia Formation are an extension of the depositional environments in the upper parts of Mashaba Formation. By the end of the Lower Jurassic, Shusha Formation is dominated by intercalations of clastic and carbonate beds of more continental sedimentary environments than Rajabia Formation (Zaki 1996; Kassab et al. 2016).

The studied Lower Jurassic formations (665 m) vary greatly in thickness from place to place even in Gebel El-Maghara area due to its structural control and setting and lateral facies changes (Moustafa and Khalil 1990; Abdelhady and Fürsich 2015; Nabawy and Abd El Aal 2019a). Their lithostratigraphy interrelationships are described as follows.

2.1 Mashaba Formation (100 m, Hettangian)

It forms the basal rocks of the Jurassic exposures in Sinai and well represented at Wadi Sad El Mashaba, 1.5 km south of Shushat El Maghara village. It is composed of 100 m of ill-sorted, coarse to fine-grained, and large tabular cross-bedded sandstones interbedded with clays and sandy limestone interbeds. Mashaba Formation is characterized by mottled appearance due to its high content of iron oxides that are represented by hematite and pyrite content (Jenkins et al., 1982; Yussef, 1986).

2.2 Rajabia Formation (293 m, Sinemurian-Pliensbachian)

Rajabia Formation outcrop is located at Wadi Rajabia and Wadi Sad El-Mashaba areas; its lithostratigraphic sequence is similar to the Mashaba Formation. Its basal and upper parts are composed of interbedded sequence of brownish sandstones and yellow marl; whereas its middle parts are composed of dolomitic limestone rocks intercalated with few thin sandstone and sandy limestone beds. However, the upper and middle part of Rajabia Formation contains more claystone and shales intercalations than its basal parts and the Mashaba Formation (Fig. 2).

2.3 Shusha Formation (272 m, Pliensbachian-Toarcian)

The type section of Shusha Formation is in the midway between Shushat El-Maghara and Wadi Mahl in Gebel El-Maghara area. It mostly consists of clastic sedimentary intercalations of cross-bedded continental sandstones, clays and shales, which are intercalated with some shallow marine limestones interbeds, especially at its lowermost parts. Its shale interbeds contains some sideritic concretions vary in thickness from few cm to 2 mm giving them their dark brown appearance. The top parts of this formation are characterized by yellowish brown hard sandstones interbedded with some shale intercalations.

3. Methodology

Some field trips were conducted to study the lithostratigraphy and geologic setting of the Lower Jurassic sequence at Gebel El Maghara area, where 100 representative surface block samples were collected and oriented horizontally parallel to the bedding plane.

To perform the petrophysical measurements, 56 representative plugs were obtained representing the different levels and lithologies of the collected blocks samples (21 plugs for Rajabia, 18 for Shusha, and 17 plugs for Mashaba formations). The studied plugs were cleaned with flushing water under vacuum to remove the fine cuttings and the soluble materials, and then dried at a temperature not more than 60° C for 48 hours in an electric oven.

The cleaned and dried plugs were weighed (w_{dry}, in g) and their bulk volume (v_b, in cm^3) was then estimated using a digital micrometer to estimate bulk density (σ_b).

σ_b (g/cm^3) = w_{dry} / v_b

Porosity was measured using helium injection and water saturation techniques. The water porosity is measured by evacuating the different samples using vacuum pump then injecting them by water and weight of the saturated samples was measured (w_{sat}, in g).

$\emptyset_W = 100 \times v_p / v_b$

$= 100 \times (w_{sat} - w_{dry}) / v_b$

Where, v_p is the total volume of pore spaces

The grain volume (v_g) is then measured using a pycnometer technique by injecting helium at 19 psi and the grain density (σ_g) and helium porosity ($\emptyset_{He}$) are calculated as follows.

σ_g (g/cm^3) = w_{dry} / v_g

$\emptyset_{He} = 100 \times v_p / v_b$

$= 100 \times (v_b - v_g) / v_b$

Water has less ability than helium to invade into the micro and nano pore spaces, so the helium porosity ($\emptyset_{He}$) is always more than or rarely equals to the water porosity ($\emptyset_{He}$). The difference between $\emptyset_{He}$ and $\emptyset_W$ represents the inaccessible pores that water can invade them (Nabawy, 2018). It can be estimated as follows:

$\emptyset_{inacc} = 100 \times (\emptyset_{He} - \emptyset_W) / \emptyset_{He}$

Permeability (k) was estimated using air permeameter, as samples were plugged in a Hassler-type core holder and k was estimated using the following equation.

$k = (Q.\mu.L) / (\Delta P.A)$

where; Q is the flow rate, μ is the air viscosity, A is its cross sectional area, L is the plug length, and ΔP is the applied differential pressure.

For reservoir quality ranking, the concept of Amaefule et al. (1993) on the hydraulic flow unit (HFU) was applied, where the HFU quality is based on the normalized porosity index (NPI), reservoir quality index (RQI), and the flow zone indicator (FZI). Each HFU is the sum up of group of samples having the same range of porosity (∅), permeability (k), RQI and FZI values. These HFU quality parameters can be estimated as follows.

NPI = ∅ / (1 - ∅)

RQI = $0.0314 (k / ∅)^{1/2}$

FZI = RQI / NPI

= $(0.0314 (k / ∅)^{1/2}) / (∅ / (1 - ∅))$

More details on the applied reservoir quality parameters were published by Nabawy and ElHariri (2008) and Nabawy et al. (2018).

For rock typing, the common porosity-permeability X-Y plot, and quality parameters, the discrete rock typing (DRT) technique of Shenawi (2007) was applied. The DRT equation was modified by El Sharawy and Nabawy (2018), and further modified as follows.

DRT = Round (2 x Ln FZI + 10.6;1)

The electric conductivity (σr) of the studied samples was measured using LCR Hi-Tester meter at three NaCl saline concentrations (10, 50, and 100 kppm, σ_W = 1.79, 9.09, and 16.7 S/m, respectively), and the true formation resistivity factor (FRT) of each plug was estimated following Nabawy and Wassif (2017), Nabawy (2018), and El Gendy et al. (2020).

The predominant diagenetic factors and mineralogy were checked petrographically; where 100 thin sections were prepared representing the collected block samples. These were impregnated with Araldite dyed blue to enable visual porosity estimation. To discriminate between calcite and dolomite, thin sections were stained Red using Alizarin Red S. Dyed and stained thin section were then studied using polarized microscope supported with a PC monitor to enable monitoring the different components, detailed studies, and precise imaging.

To image the pore spaces in details, to reveal the predominant digenetic factors, and to check clay types and distribution, 15 representative rock fragments were coated by gold and scanned using scanning electron microscopy (SEM). The SEM Model QUANTA FEG250 was applied with accelerating voltage 200v-30kV, and magnification 30X-300kX.

Finally, to estimate the different mineral components of the studied rock types in semi-quantitative way, ten representative samples were selected form the studied samples and prepared as very fine powder for X-ray diffraction analysis (XRD). Analysis was applied using a Philips X-ray diffractometer supported with Ni-filtered Cu radiation at 40 KV and 30 MA, in the range 2θ = 5–80° and scanning speed of 0.01°/sec.

The X-ray data analysis was performed using ASTM cards and compared with the data published by Brown (1961), where a semi-quantitative estimation of the different mineral components of the studied rock types has been assigned.

4. Results

4.1 Reservoir Rock Types (RRTs)

Based on the discrete rock type (DRT) values and the other petrophysical parameters, the Lower Jurassic sequence in north Sinai at Gebel El-Maghara area is subdivided into three reservoir rock types (RRTs). The RRT is highly porous and permeable with good reservoir quality; it has very good average helium porosity (2.3 %), good water porosity (16.4 %), very good permeability (129.9), fair reservoir quality index (0.68 µm), poor flow zone indicator (2.31 µm), relatively high DRT values (12.2), and meso effective pore radius R_{35} (5.72 µm, Table 1). Its average RQI and FZI values are fair and poor values with fair reservoir rank.

Table 1
Storage and flow capacity core data and reservoir quality parameters of the different rock types RRTs of the Mt Messenger Formation.

RRT	MFA		k	$\emptyset_{He}$	$\emptyset_W$	σ_g	σ_b	R_{35}	RQI	FZI	DRT	RQI_{rank}	FZI_{rank}	Reservoir	Pore Size
			md	**%**	**%**	**(g/cc)**	**(g/cc)**	**µm**	**µm**	**µm**	**0.0**	**0.0**	**0.0**	**rank**	
RRT1	**MFA1**	Min	15.7	14.20	10.6	2.61	1.87	2.74	0.33	1.58	11.8	3	3	Poor	Meso
		Max	405.7	28.91	22.6	2.70	2.31	10.1	1.18	3.01	12.8	5	5	Fair	Macro
		Average	129.9	22.32	16.4	2.66	2.06	5.72	0.68	2.31	12.2	4	5	Fair	Meso
RRT2	**MFA2**	Min	0.95	7.36	4.26	2.68	2.44	0.88	0.11	1.28	11.0	6	5	Tight	Micro
		Max	3.65	9.57	6.55	2.71	2.49	1.64	0.19	1.63	11.7	6	5	Tight	Meso
		Average	1.83	8.30	5.46	2.69	2.47	1.19	0.14	1.47	11.4	6	5	Tight	Meso
RRT3	**MFA3**	Min	0.025	2.19	1.19	2.65	2.44	0.25	0.03	0.46	9.1	6	5	Tight	Micro
		Max	0.343	9.71	6.26	2.71	2.63	0.45	0.06	1.07	11.0	6	6	Tight	Micro
		Average	0.130	5.70	3.61	2.69	2.53	0.34	0.04	0.74	10.1	6	6	Tight	Micro

where; k is the gas permeability $\emptyset_{He}$ & $\emptyset_W$ are the helium and porosity, respectively; σ_g & σ_b are the grain and bulk densities, respectively; R_{35}, is the pore radius of the studied samples at 35 % mercury saturation; RQI, is the reservoir qulaity index; FZI, is the flow zone indicator; DRT, is the discret rock type; RPI, is the reservoir potentiality index. Ranks of RQI, FZI and pore size are based on the ranking values that proposed by Nabawy et al. (2018), and Elgendy et al. (2020). RRT and MFA are the reservoir rock type and microfacies association, respectively.

The RRT3 is a tight rock type with very low porosity, permeability, RQI, FZI, DRT, and R_{35} values (av. $\emptyset_W$ = 3.61 %, av. $\emptyset_{He}$ = 5.7 %, k_{av} = 0.13 md, RQI_{av} = 0.04 µm, FZI_{av} = 0.74 µm, DRT_{av} = 10.1, and av. R_{35} = 0.34 µm). It is ranked as tight reservoir with tight RQI and FZI and micro effective pore radius (Table 1).

The RRT2 is a transitional group between the RRT1 and RRT3 samples with midway petrophysical properties (av. $\emptyset_W$ = 5.46 %, av. $\emptyset_{He}$ = 8.3 %, k_{av} = 1.83 md, RQI_{av} = 0.14 µm, FZI_{av} = 1.47 µm, DRT_{av} = 11.4, and av. R_{35} = 0.34 µm, Table 1).

The FR_T (true formation resistivity factor) values of RRT1 plugs varies from 41.3 to 523.8 of average FR_T = 169.8, whereas the average FR_T of the RRT3 equals 473.1(Table 2). The constant porosity exponent (m) is lower for RRT3 than that of RRT1 plugs, and also the variable porosity exponent (m') is lower for the tight RRT3 samples ($1.60 \leq m' \leq 1.88$, m'_{av} = 1.72) than that for the porous and permeable RRT1 samples ($2.45 \leq m' \leq 2.91$, m'_{av} = 2.66, Table 2).

Table 2
Electric properties of the studied samples.

RRTs	MFA		FR_T	$\emptyset_W$	a	m	m'
			0.0	**%**	**0.0**	**0.0**	**0.0**
RRT1	**MFA1**	Min	41.3	10.6			2.45
		Max	523.8	22.6	1.14	2.60	2.91
		Average	169.8	16.4			2.66
RRT2	**MFA2**	Min	243.9	4.26			1.98
		Max	556.3	6.55	2.57	1.70	2.13
		Average	381.5	5.46			2.06
RRT3	**MFA3**	Min	99.6	1.19			1.60
		Max	1225.0	6.26	2.05	1.48	1.88
		Average	473.1	3.61			1.72

where; FRT is the true formation resistivity factor; a is the lithology factor, m is the fixed porosity exponent, and m' is the variable porosity exponent. RRT and MFA are the reservoir rock type and microfacies association, respectively. The FR_T classification ranks are following Nabawy (2018).

4.2 Microfacies Analysis

To reveal the mineral composition of the available Lower Jurassic samples and to reveal the dominant diagenetic factors that control the reservoir quality of this sequence in its surface type section, a detailed microfacies analysis was applied. Also, discriminating the samples into some microfacies association (MFA) will explain the variation in the petrophysical properties of the assigned RRTs. Following rock typing, three microfacies associations (MFAs) were assigned for the studied samples. Each is characterized by some distinctive visible aspects that are identifiable by the petrographical studies, and represents the mineral composition and microfacies of each corresponding RRT.

4.2.1 Microfacies Association MFA1 (RRT1)

This microfacies association represents the mineral composition, and pore types of the RRT1 samples. It is mostly represented through the Shusha and Rajabia formations.

Siliceous Quartz Arenite

It represents the top parts of Shusha and Rajabia formations; it consists of very fine to fine, well-sorted, and sub-rounded to sub-angular quartz grains and feldspars cemented together by meniscus silica cement and quartz overgrowth with very good visual porosity ($\emptyset \geq 20$ %). Pore spaces are mostly described as: 1) intergranular pore spaces, slightly reduced by iron oxide patches (Fig. 3a), 2) micro to meso vugs, and 3) microfractures (Fig. 3a).

Ferruginous Kaolinitic Siliceous Quartz Arenite

It also represents the top parts of Rajabia Formation; it consists of medium-sorted fine to very fine angular monocrystalline quartz grains with some feldspars cemented by silica cement (Fig. 3b). Compaction is indicated by concave-convex, suture and point grain contacts, and wavy extinction (Fig. 3b). The quartz grains are commonly corroded by the cement increasing the grain angularity. A noticeable amount of silt sized-grained iron oxides, and kaolinite patches are disseminated in between quartz grains to support the microsparite cement in reducing the total connected pore volume. This iron content gives the samples their diagnostic brownish yellow colour. The interstitial pore spaces are described as: 1) intergranular pores, frequently reduced by kaolinite, silica and iron oxides (Fig. 3b), 2) micro vugs (Fig. 3b), and 3) microfractures. The estimated visual porosity is good to fair and varies between 10 and 20%.

Ferruginous Dolomitic Packstone

It represents the middle parts of both Shusha and Rajabia formations. It is composed of highly porous micrite with some sparite, pseudo sparite, dolomicrite and dolomicrosparite (Fig. 3c). Few clastic components and allochems are assigned in the groundmass, besides to many sparite-filled fossil molds are assigned. Iron oxide and clay patches are scattered within the groundmass. Though invading this microfacies by Ca-bearing solution and filling many pore spaces, it has good to very good visual porosity (15–20%). Pores are described as: 1) micro intercrystalline pores, 2) meso to micro vugs, sometimes filled by sparite and pseudo sparite, 3) sparite-reduced moldic porosity, 4) microfractures, partially reduced by microsparite, and 5) meso to micro channels partially filled by microsparite (Fig. 3d).

4.2.2 Microfacies Association MFA2 (RRT2)

This association is composed of only one clastic microfacies, ferruginous kaolinitic and sparitic quartz arenite, forming the top parts of Shusha Formation.

Ferruginous Kaolinitic and Sparitic Quartz Arenite

It consists of medium to fine-grained, moderately sorted, and sub-angular to sub-rounded quartz grains cemented by sparite cement (stained red, Fig. 3e). The quartz grains are slightly compacted together and corroded by the sparitic cement with many dull spots of iron oxides and clay patches. Compaction is also indicated by presence of some fractured quartz grains and quartz overgrowth (Fig. 3e). Petrographically, the visual porosity is slightly reduced than the first MFA1 and ranked as poor to good (5–15 %). Pores are discriminated into: 1) micro intercrystalline pores, reduced by pseudo sparite cement, 2) meso vugs (Fig. 3e), and 3) microfractures.

4.2.3 Microfacies Association MFA3 (RRT3)

It is relatively compacted and tight MFA composed of many clastic and non-clastic microfacies representing the basal parts of Shusha and Rajabia formations, and most parts of Mashaba Formation.

Highly Ferruginous and Sparitic Quartz Arenite

This tight microfacies consists of very fine to fine, well sorted, sub-rounded to sub-angular quartz grains cemented by pseudo sparite to microsparite. The quartz grains are compacted together through point and straight grain to grain contact (stained red, Fig. 3f). Few very fine allochems fragments and much iron oxide grains are discriminated through the cement (Fig. 3g). Porosity of this microfacies is negligible (2–8%) and is mostly described as: 1) micro intercrystalline pores, 2) microfractures, and 3) micro vugs (dyed blue, Fig. 3f).

Highly Compacted Siliceous Lithic Arenite

It represents the topmost parts of Mashaba Formation; it consists of poorly sorted, pebbly sized to fine grains, angular to sub-angular highly compacted quartz grains cemented by silica cement (Fig. 3f). It is characterized by many lithic/rock fragments aligned in streaks in alternation with fine to very fine quartz grains. Compaction is indicated by point, straight, and suture contacts, wavy extinction, with some fractured quartz grains. Porosity is highly obliterated (ϕ < 5 %) due to the compaction and silica cementation. Pores are represented by: 1) micro intergranular pores highly reduced by silica cement, and 2) microfractures.

Highly Fractured Bioclastic Wackestone

Its groundmass consists of micrite with few disseminated microsparite patches. This Highly fractured bioclastic wackestone microfacies contains some well-preserved fossils and fossil remains represented by pelecepods, brachiopods, and foraminifera (Fig. 3i). It is characterized by presence of many intersected sealed microfractures (Fig. 3i, j), mostly sealed, indicating suffering from severe compaction and cementation episodes. Visual porosity is highly reduced to negligible values (ϕ < 5 %) and described as: 1) micro intercrystalline pores, 2) pseudo sparite-reduced micro vugs, and 3) microsparite-reduced microfractures (Fig. 3j).

Fractured Bioclastic Packstone

This microfacies is similar to the highly fractured bioclastic wackestone microfacies but with less sealed fractures and more developed crystals with some dull clay, sparite and pseudo sparite patches. Some allochems are disseminated within the groundmass; sometimes are replaced by well-developed sparite crystals with some preserved fibrous micritization at the borders (Fig. 3k). Besides, some channels are assigned filled with well-developed drusy sparite crystals (Fig. 3l). Visual porosity is highly obliterated (ϕ < 5 %) due to a prolonged phase of cementation by sparite. It is characterized by: 1) micro intercrystalline pores, 2) macro to meso sparite-filled molds (Fig.

4.3 Authigenic Minerals

Authigenic minerals including types and distribution of clay minerals and iron oxides can be studied in details using the scanning electron microscopy (Nabawy and Abd El Aal, 2019b). These accessory minerals and their distribution are the main diagenetic control for the reservoir quality (Nabawy et al., 2019, 2020).

4.3.1 MFA1

The siliceous quartz arenite and ferruginous kaolinitic siliceous quartz arenite microfacies of MFA1 are affected by kaolinite clay content which is assigned filling the pore channels which slightly reduced the pore volume of the siliceous quartz arenite and moderately affected the ferruginous kaolinitic siliceous quartz arenite microfacies (Fig. 4a). It is aligned filling the pore spaces and attached to their walls. Also, presence of few illite clay patches (Fig. 4b), and some patches of rose and sea star-shaped iron oxides stained the samples with its brownish colour and slightly reduced the pore volume (Fig. 4c). The SEM studied indicated dissolution of some sparite crystals of the ferruginous dolomitic packstone microfacies of Shusha which helped in enhancing its reservoir quality. This phenomenon is represented by pitted surface and hollow crystals (Fig. 4d).

However, due to their low swellability, implementation of the present kaolinite and iron oxide content is not enough to reduce visual porosity which varies between 15 and 30 % (Fig. 4a-d).

4.3.2 MFA2

As the case of the MFA1 microfacies, the ferruginous kaolinitic and sparitic quartz arenite samples of Shusha Formation is affected by the kaolinite clay content which filled the pore channels and affected the total pore volume of this microfacies (Fig. 4e). Also, the pore spaces are filled with some iron oxides in the form of star shape (Fig. 4f), which accumulated with the kaolinite booklets to reduce the pore connectivity (Fig. 4g). Filling the pore spaces with patches of the iron oxides helped the diagenetic cementation by sparite to reduce the visual porosity of the studied microfacies (Fig. 4h).

4.3.2 MFA3

The last microfacies association is mostly composed of tight, compacted, and well cemented microfacies. This due to quartz overgrowth and filling the pore spaces by well-developed dolomite and sparite crystals (Highly Compacted Siliceous Lithic Arenite, Fig. 4i). Beside to the tight cementation, presence of illite fibers and kaolinite booklets highly reduced the connected pore spaces of the highly ferruginous and sparitic quartz arenite microfacies (Fig. 4j). The illite fibers and star-like iron oxides are embedded within the cement indicating that forming of these authigenic minerals is prior to the final stage of cementation by sparite (Fig. 4k, l).

4.4 X-ray Diffraction Studies

Samples of the Lower Jurassic Mashaba, Rajabia, and Shusha formations are composed of carbonate and sandstone intercalations, represented by quartz (SiO_2), and calcite ($CaCO_3$) with few dolomite ($Mg.Ca(CO_3)_2$) and kaolinite ($Al_2Si_2O_5(OH_4)$) content (Table 3). Also, few iron contents of goethite ($FeO(OH)$) and hematite (Fe_2O_3) are present with traces of Gypsum ($CaSO_4.2(H_2O)$). The analyzed Mashaba samples are mostly composed of calcite mineral assigned ($2\theta = 29.42°$, Fig. 5a) Upwards through Rajabia and some intercalations in Shusha formations, the non-clastic

composition is replaced by sandstones that composed of quartz (2θ = 26.65°) with few plagioclase (Fig. 5b, c). Some ferruginous (12.4 ≤ hematite ≤ 29.5%) sandy limestone and calcareous sandstone are assigned in Rajabia and Shusha formations, respectively. Some goethite and kaolinite contents are also present in the studied two formations (Table 3).

Table 3
Relative proportions of the different mineral components of the Lower Jurassic formations in Gebel El-Maghara area obtained from the XRD analysis.

Formation	S. No.	Quartz	Plagioclase	Calcite	Dolomite	Kaolinite	Goethite	Hematite	Gypsum
Mashaba	Ma1	—	—	94.5	0.51	1.4	0.12	2.28	1.20
	Ma2	—	—	77.3	8.15	9.1	5.1	0.35	—
	Ma3	—	—	71.8	6.69	11.2	6.3	4.01	—
Rajabia	Rg1	97.6	2.4	—	—	—	—		—
	Rg2	89.2	9.4	—	—	—	—	1.4	—
	Rg3	—	12.6	54.1	—	3.8	—	29.5	—
Shusha	Sh1	—	12.2	23.4	—	2.2	—	1.7	—
	Sh2	—	—	1.4	—	1.5	5.0	0.8	—
	Sh3	50.4	—	27.3	—	9.9	—	12.4	—
	Sh4	83.9	—	16.1	—	—	—	—	—

5. Discussion

5.1 Implementation of diagenetic controls on the petrophysical properties

The reservoir parameters are controlled by the mineral composition and the pore and rock fabrics of rock samples which are represented by their microfacies types. For this research article, the plug samples are subdivided into 3 RRTs, each with its diagnostic microfacies association (MFAs).

5.1.1 MFA1 (RRT1)

Dominance of the reservoir quality-enhancing diagenetic controls including dissolution of cement and allochems (Fig. 3a), and fracturing (Fig. 3d) increased the storage and flow capacities of the RRT1 samples with fair to excellent porosity and permeability (Table 1). Also, impacts of the reservoir quality-reducing diagenetic controls are limited. These are represented by slight compaction leads to some grain fracturing and point contact grain to grain relationship (Fig. 3a). Cementation by the intercrystalline pore spaces and vugs by sparite, invading and filling the pore channels by micro and pseudo sparite partially reduced the pore volume, but still there is a 15–20% visual porosity (Fig. 3c, d). Even though, presence of some iron oxides and authigenic clay minerals (Fig. 4a-c), their impact is also limited to block few vugs and to line some pore walls.

5.1.2 MFA2 (RRT2)

The reducing impact of diagenetic factors on reservoir parameters of the ferruginous dolomitic packstone samples is effective, where cementation by sparite and dolomite is dominant and more implemented than that for the MFA1 samples. Accumulation of high amount of kaolinite and iron oxides in the pore spaces blocked some pore throats and reduced the pore connectivity (Figs. 3e-g, 4e-h). In comparison to the MFA1 (RRT1) and MFA3 (RRT3), implementation of the reservoir quality-reducing factors is moderate, so the MFA2 (RRT2) samples are a transitional group between the RRT1 and RRT3 samples.

5.1.3 MFA3 (RRT3)

This group of samples has the lowest reservoir quality in the studied Lower Jurassic samples in Gebel El-Maghara area. It is highly cemented by sparite and dolosparite (Fig. 4i). Impacts of the reservoir quality-enhancing factors including fracturing and dissolution are obliterated by cementation (Fig. 3i-l). It is also suffered from severe compaction which supported cementation in reducing the total pore volume. The authigenic minerals filled and blocked the pore channels in between the cement and matrix which seem to be supported by later phase of calcite cementation that tightly blocked some pore spaces (Fig. 4l).

5.2 Porosity-density relationships

Two types of densities are assigned, the grain density (σ_g) which is a function of the mineral composition and the bulk density (σ_b) which is controlled by the grain density and porosity. Plotting the grain and bulk densities on X-Y plot indicates that most of RRT1 plugs have grain densities between 2.65 g/cm^3 (quartz line) and 2.71 g/cm^3 (calcite line, Fig. 6a). The siliceous quartz arenite and the ferruginous kaolinitic siliceous quartz arenite RRT1 samples are characterized by grain density around the quartz line at 2.65 g/cm^3. Shifting the grain density to values higher than the

quartz line is due to the calcitic composition of the carbonate microfacies in the MFA3 and the ferruginous dolomitic packstone of the MFA1 samples, whereas increasing the grain density of the clastic microfacies (the ferruginous kaolinitic siliceous quartz arenite of MFA1, ferruginous kaolinitic and sparitic quartz arenite of MFA2, and the highly compacted siliceous lithic arenite of MFA3) is attributed to increasing their sparite, dolomite and iron oxides content (Figs. 3e-g, 4c, g, i). The 2.71 g/cm^3 bulk density line separates the RRT1 samples from that of the other two RRTs which is attributed to their fair to excellent porosity values (Fig. 6a). This plot is supported by plotting the helium porosity ($\emptyset_{He}$) as a function of the bulk density which indicates that porosity values of the RRT1 samples is higher than that of the other two RRTs. Porosity of the RRT1 samples is mostly higher than 15 %, whereas porosity of the RRT2 and RRT3 are less than 10 % (Fig. 6b). The high reliability of the obtained best-fit line for the different rock types ($R^2 \geq 0.921$, Fig. 6b) is a good proof for quality of the petrophysical measurements. Due to the similar multiplication factors and constants of the obtained RRTs' porosity-density models (Fig. 6b), a model can be applied to estimate the helium porosity of all plugs in terms of their bulk densities as follows.

$\emptyset_{He} = -35.2\ \sigma_b + 95.0$ ($R^2 = 0.995$)

For the electric measurements, samples were saturated with saline and water porosity was estimated for the samples. Data of the $\emptyset_W$-σ_b plot are scattered ($R^2 < 0.73$, Fig. 6c) and less reliable than that of the $\emptyset_{He}$-σ_b ($R^2 > 0.92$, Fig. 6b), i.e., its indication for the bulk density is less than that of the helium porosity and. This can be attributed to the fact that, water has less ability than helium to invade the micro and nano pores, so the water porosity ($\emptyset_W$) is mostly less than that of the helium porosity (Fig. 7m Table 1). The more shifts toward the helium porosity Y-axis on the $\emptyset_{He}$-$\emptyset_W$ plot indicates presence of more micro and nano pores that the water cannot invade. A set of reliable mathematical equations ($0.641 \leq R^2 \leq 0.742$) were introduced to estimate the $\emptyset_{He}$ and $\emptyset_W$ in terms of each other (Fig. 7).

5.3 Contribution of porosity to permeability

Permeability and porosity are the main controls for reservoir quality; they define the reservoir storage and flow capacities. Plotting permeability versus helium porosity indicates three different petrophysical behaviors; RRT1 samples have the highest storage and flow capacities (very good to good permeability, and excellent to fair permeability values), whereas RRT3 samples are tight to poor (tight to poor porosity and permeability values). A set of reliable models were introduced to estimate permeability as a function of the helium porosity (Fig. 8). Similarity in the porosity exponent of the k-$\emptyset_{He}$ is due their dominant clastic composition, whereas the RRT3 are mostly composed of carbonate microfacies.

5.4 Reservoir quality controlling factors

The reservoir quality concept, including the RQI and FZI parameters, has been introduced by Amaefule et al. (1993) and checked for ranking the clastic and non-clastic reservoirs by many researchers (e.g., Tiab and Donaldson, 1996; Corbett and Potter, 2004; Al-Dhafeeri and Nasr-El-Din, 2007; Teh et al., 2012; Abed, 2014; Nabawy and El Sharawy, 2015, 2018; Nabawy et al., 2018). These reservoir quality parameters are estimated as a function of porosity and permeability, so they are reasonable are factors of these two parameters ($\emptyset$ and k). Plotting the RQI versus permeability (Fig. 9a) indicates that the RQI is mostly controlled by the permeability as an indicator for the flow capacity of the reservoir. Factors and exponents of the RQI-k models of the RRT1 and RRT2 groups are similar with tight quality for RRT2 plugs and poor to good reservoir quality for RRT1 plugs (Fig. 9a). This should be attributed to the fact that cementation and filling pores with authigenic clay and iron oxides are more effective for the RRT2 than the RRT1. Tightness, well cementation, and blocking the pore channels by calcite cement are the main reason for the tight RQI values of the RRT3 samples (Figs. 3i-l, 4k-l, Fig. 9a). Due to the high reliability of the obtained RQI-k mathematical models and similarity in the multiplication factors and exponents, a general model is applied to estimate permeability in terms of their RQI values as follows.

$RQI = 0.11\ k^{0.39}$ ($R^2 = 0.994$)

Dependence of the RQI on porosity values is less than its dependence on permeability, where the reservoir quality is a direct measure of how much the reservoir porosity contributes to its permeability, i.e., it is a measure for the most effective and permeable porosity not all the connected pore spaces. So, its dependence on porosity is based on the amount of connected pore spaces, where reliability of the RQI-$\emptyset_{He}$ model is higher for the more porous RRT samples (Fig. 9b). No reliable models can be obtained for the RQI with the $\emptyset_{He}$ values of the tight RRT3 samples. This may be explained by the higher complexity and the lower connectedness of its pores than the other two RRTs.

On the other side, due to the effect of the normalized porosity index (NPI) values on the flow zone indicator (FZI) values, the relationship between the FZI values and the reservoir parameters are less consistent than those relationships with the RQI. No relationships can be established between the FZI and $\emptyset_{He}$ values for the different RRTs, whereas two moderately reliable models were established between the FZI and k for the RRT1 and RRT2 samples ($R^2 \leq 0.559$) with scattered samples for the RRT3. This also can be attributed to more tightness and complexity of pore throats of the RRT3 samples.

5.5 Rock typing based on FZI

Rock typing of the present study is based on the discrete rock types (DRT) which in turns based on the FZI values which is also used as a main key factor for rock typing process. Plotting permeability versus porosity is also applied as a common technique for subdividing the rock samples into some RRTs. So, the FZI values is superimposed on the k-$\emptyset_{He}$ plot as intersecting lines separating the studied samples into clusters of similar porosity

and permeability trends (Fig. 11). This plot indicates that, the RRT1 is limited by FZI lines = 1.582 and 3.011 µm, which is considered as poor to fair reservoir quality, whereas the RRT2 samples are situated between FZI lines 1.00 and 1.582 µm indicating samples of poor reservoir quality. This is due to their very good to poor permeability values, and their very good to poor porosity values. The tight RRT3 samples are characterized by FZI values less than 1.00 µm (Fig. 11).

On the other side, superimposing the FZI lines on the RQI-NPI plot supports this achievement, and indicates that only the RQI values of the RRT1 samples are accepted for poor to good reservoir quality ($0.33 \leq RQI \leq 1.18$ µm, Fig. 12a, Table 1).

Plotting the RQI values versus the FZI values of the different RRTs indicates that, the RRT1 samples have good to poor RQI and FZI values, i.e., accepted as reservoir rocks in its subsurface extensions. The RRT3 plugs of the MFA3 are compact, tight, and characterized by tight RQI and FZI values. The RRT2 samples are transitional between these two RRTs, and though they have poor FZI values their values indicate tight reservoir (Fig. 12b). This may be explained by the double effect of porosity values, firstly on NPI values and then on the FZI values (El Sharawy and Nabawy, 2018, 2019).

5.6 Impacts of porosity on the true formation resistivity factor (FR_T) and Archie's parameters

The FR_T is mostly controlled by the effective water porosity ($\emptyset_W$), the mineral composition, and the pore and rock fabrics. Plotting the FR_T versus $\emptyset_W$ declares that, the RRT1 which is composed of the MFA1 (mostly porous clastics) are characterized by the highest porosity (av. $\emptyset_W$ = 16.4 %) and the lowest FR_T values (av. FR_T = 169.8, Table 2, Fig. 13), whereas the RRT3 samples are composed of mostly tight rocks of MFA3 which are characterized by the lowest porosity (av. $\emptyset_W$ = 3.63 %) and the highest FR_T values (av. FR_T = 473.1, Table 2, Fig. 13). Therefore, due to its tightness and pore fabric complexity, the RRT3 samples are characterized by high average FR_T value = 473.1 (300 < high $FR_T \leq$ 500, Nabawy, 2018), whereas due to the pore connectedness the RRT1 samples are characterized by medium average FR_T value = 169.8 (150 < medium $FR_T \leq$ 300, Nabawy, 2018). It is indicated that, increasing the water porosity is accompanied by decreasing the FRT, i.e., they are inversely related to each other (Fig. 13). To check Archie's parameters, m and a (porosity exponent, and lithology/tortuosity factor, respectively), two methods of statistical processing are applied: 1) free regression with a constant m value, and 2) fixed regression with variable m values (m') (El Sharawy and Nabawy, 2018). For the first method, FR_T values of each RRT are plotted versus their corresponding $\emptyset_W$ and are processed as one set of samples to get its diagnostic tortuosity factor (a), and its porosity exponent (m) (Fig. 13). A set of reliable mathematical models are obtained to calculate the FR_T versus $\emptyset_W$. Increasing the porosity values of RRT1 plugs is accompanied by increasing the Archie's porosity exponent (m = 2.60), whereas the tight RRT3 samples have the lowest m (m = 1.48, Fig. 13). To get more detailed information about the porosity exponent, the second method (fixed regression) is applied to the studied samples assuming a = 1 to get variable m (m') which changes from sample to sample with the highest m' samples are assigned to the highly porous RRT1 samples and the lowest m' values for the tight and compacted RRT3 samples (Table 2). Plotting the m' values for the different RRT samples indicate that m' is directly proportional of the water porosity. A set of mathematical models can be obtained to calculate the m' using the water porosity (Fig. 14). This achievement is corresponding with that obtained by Nabawy (2018), where m is directly proportional to $\emptyset_W$.

Due to differences pore connectivity, and variation in the electric effectiveness and sharing of the iron oxides and clay content (based on their amounts and type of distribution), no model can be obtained to estimate the FR_T of all RRTs in terms of their $\emptyset_W$.

5.7 Reservoir Zonation and Hydraulic Flow Units (HFUs)

Subdividing the reservoir sequence into some HFUs is required for getting a precise reservoir modeling, each HFU with its diagnostic model. The HFU is a common concept referring to a cumulative sequence of similar flow capacity and petrophysical properties in a given reservoir. Its petrophysical properties are internally consistent, but easily recognized from that of the overlying and underlying units. The reservoir rock typing is based on some X-Y plots and the depth is not taken into consideration, but the HFU concept is based on plotting the different petrophysical parameters versus depth (Nabawy et al., 2019; Abuamarah et al., 2019). It has been tested and applied by many authors (e.g., Ebanks et al., 1987; Ti et al., 1995; Martin et al., 1997; Aminian et al., 2003; Orodu et al., 2009; Abde, 2014; Kassab et al., 2016, 2017; Abdulelah et al., 2018).

Plotting porosity ($\emptyset_{He}$, $\emptyset_W$), inaccessible porosity ($\emptyset_{Inacc}$), permeability, FR_T, RQI, FZI, and the R_{35} of Winland (1972) as a function of depth, enabled assigning five HFUs in the studied Lower Jurassic sequence. Each unit is characterized by its internal consistent petrophysical properties and is easily predicted from the surrounded units (Fig. 15). As shown in Fig. 15, and based on arbitrary cutoff values ($\emptyset_{cutoff}$ = 10 %, k_{cutoff} = 1.0 md, RQI_{cutoff} = 0.25 µm, FZI_{cutoff} = 1.0 µm, $R_{35,\ cutoff}$ = 1.0 µm), it is indicated that the whole sequence of Rajabia Formation, and middle parts of Shusha Formation are prospective units represented by HFU-2 and HFU-4, respectively. These two prospective units are mostly composed of the first and second microfacies association (MFA1 and MFA-2, respectively). The HFU-2 consists of the RRT1 samples which are characterized by $\emptyset_{He}$ in the range 20–30%, with higher values for the lower carbonate part. Selective and partial dolomitization enhanced and supported the prospective petrophysical properties of this sequence which is composed mostly of ferruginous dolomitic packstone microfacies. The upper parts of Rajabia (top of HFU2), and the HFU4 in Shusha formations are consists of the siliceous quartz arenite and the ferruginous kaolinitic siliceous quartz arenite microfacies (RRT1) which are porous and permeable microfacies. Due to filling pores and cementation with sparite and pseudo sparite the reservoir prospectivity of the top parts of HFU4 (ferruginous kaolinitic and sparitic quartz arenite microfacies, MFA2, RRT2) is slightly reduced. Separation between the

water and helium porosities (track-1, Fig. 15) is due to presence of some micro and nano pores that water cannot invade, i.e., the high separation indicates higher inaccessible pore percentage (Track-2). Due to the high effective porosity of these two HFUs, permeability values are mostly higher than 10md (Track-3), the RQI and FZI values are higher than their cutoff values (Track-5) with the effective pore radius R_{35} more than 1.0 µm (meso pores, Track-6, Fig. 15).

Due to complexity of the pore throat distribution and diagenesis, and the bad pore connectivity, the basal parts of the section, Mashaba Formation (HFU-1), basal and top parts of Shusha Formation (HFU-3, HFU-5) an intensive fluctuation of the inaccessible pore percentages is assigned with very low porosity, permeability, RQI and FZI, and micro pore sizes (R_{35} < 1.0 µm).

Increasing the FR_T values (Track-4) of the Mashaba Formation is due to its tight cementation, very low porosity values, and complexity of pore throats. Fluctuation of these electric values is comparable to their corresponding water porosity and effective pore radius (Fig. 15).

For subsurface exploration of the area in vicinity (offshore marine exploration in the Mediterranean Sea), it is recommended to follow up the Rajabia Formation and top parts of Shusha Formation. On the other side, due to the very low porosity values of Mashaba Formation, tightness, fossil content, and beauty appearance, it can be used as building stones and marble tiles.

6. Conclusions

Based on their petrophysical properties, the Lower Jurassic Mashaba, Rajabia and Shusha formations in their type sections in Gebel EL-Maghara area were subdivided into five hydraulic flow units (HFUs) that consist of three reservoir rock types (RRTs). Each flow unit has its diagnostic petrophysical properties. HFU2 of Rajabia Formation is the best flow units; it consists mostly of RRT1 samples, whereas the HFU1 of Mashaba Formation is the tightest unit that is built of RRT3 plugs.

The RRT1 plugs are the most porous and permeable samples (av. $\emptyset_{He}$ = 22.3 %, and $k_{av.}$ = 29.9 md) with the best reservoir quality properties ($RQI_{av.}$ = 0.68 µm, $FZI_{av.}$ = 2.31 µm, and $DRT_{av.}$ = 12.2). This is due to dissolution and fracturing as reservoir quality-enhancing factors, and due to its dominant clastic composition. It is composed of microfacies association 1 (MFA1) which consists of: 1) siliceous quartz arenite, 2) ferruginous kaolinitic siliceous quartz arenite, and 3) ferruginous dolomitic packstone.

On the other side, due to presence of authigenic clay minerals, compaction, and tight cementation, RRT3 are characterized by the lowest reservoir quality (av. $\emptyset_{He}$ = 5.7 %, $k_{av.}$ = 0.13 md, $RQI_{av.}$ = 0.04 µm, $FZI_{av.}$ = 0.74 µm, and $DRT_{av.}$ = 10.1).

Petrographically, it is composed of MFA3 which includes: 1) Highly ferruginous and sparitic quartz arenite, 2) Highly compacted siliceous lithic arenite, 3) Highly fractured bioclastic wackestone, and 4) Fractured bioclastic packstone.

The RRT2 of Shusha Formation, which consists of ferruginous kaolinitic and sparitic quartz arenite (MFA2), is a transitional RRT between the other two RRTs. It is concluded that Rajabia Formation and few levels of Shusha Formation are considered prospective for economic fluids accumulation.

Declarations

Conflict of Interest

The authors hereby declare that they have no conflict of interest, where they didn't receive fund or grant to cover the present study. The authors confirm that they didn't receive a speaker honorarium from any companies and don't own stock in companies. In addition, all the authors are not committee members in any organizations that may causes conflict of interest.

References

Abd El Aal, A., Lelek, J.J., 1994. Structural development of the Northern Sinai, Egypt and its implications on the hydrocarbon prospectivity of the Mesozoic. The Middle East Petroleum Geosciences, Bahrain, I, 15-30.

Abdelhady, A.A., Fürsich, F.T., 2015. Quantitative biostratigraphy of the middle to upper Jurassic strata of Gebel Maghara (Sinai, Egypt). Newsletters on Stratigraphy, 48(1), 23-46.

Abdulelah, H., Mahmood, S., Hamada, Gh., 2018. Hydraulic flow units for reservoir characterization: A successful application on arab-d carbonate. IOP Conference Series: Materials Science and Engineering, 380, 012020.

Abed, A.A., 2014. Hydraulic flow units and permeability prediction in a carbonate reservoir, Southern Iraq from well log data using non-parametric correlation. International Journal of Enhanced Research in Science Technology & Engineering 3 (1), 480-486.

Abuamarah, B.A., Nabawy, B.S., Shehata, A.M., Kassem, O.M.K., Ghrefat, H., 2019. Integrated geological and petrophysical characterization of oligocene deep marine unconventional poor to tight sandstone gas reservoir. Marine and Petroleum Geology 109, 868-885.

Al-Dhafeeri, A.M., Nasr-El-Din, H.A., 2007. Characteristics of high-permeability zones using core analysis, and production logging data. J. Petrol. Sci. Eng. 55, 18-36.

Al-Far, D.M., 1966. Geology and coal deposits of Gebel Maghara, North Sinai. Geol. Surv. Egypt, 37, 59.

Amaefule, J.O., Altunbay, M., Tiab, D., Kersey, D.G., Keelan, D.K., 1993. Enhanced reservoir description: Using core and log data to identify hydraulic (flow) units and predict permeability in uncored intervals/wells. SPE 26436. Presented at the annual technical conference and exhibition, Houston, TX, 3-6.

Aminian, K., Ameri, S., Oyerokun, A. Thomas, B., 2003. Prediction of flow units and permeability using artificial neural network. Proceedings of the SPE Western Regional Meeting, May 19-24, 2003, California, USA, 297-303.

Brown, B., 1961. The X-Ray identification and crystal structures ofclay minerals. Mineralogical Society; London.

Corbett, P.W.M., Potter, D.K., 2004. Petrotyping: a base map and Atlas for navigating through permeability and porosity data for reservoir comparison and permeability prediction. In: International Symposium of the Society of Core Analysts.

Ebanks, W.J., 1987. Flow unit concepts: Integrated approach to reservoir description for engineering projects. AAPG. Bull., 71, 551-552.

El Manawi, A.H.W., 1986. Petrological and mineralogical studies of the Mesozoic ferruginous sediments of Gebel El Maghara, North Sinai, Egypt, Cairo Univ. MSc Thesis.

El Sharawy, M.S., Nabawy, B.S., 2018. Determining the porosity exponent m and lithology factor a for sandstones and their control by overburden pressure: A case study from the Gulf of Suez, Egypt. AAPG Bulletin, 102(9), 1893-1910.

El Sharawy, M.S., Nabawy, B.S., 2019. Integration of electrofacies and hydraulic flow units to delineate reservoir quality in uncored reservoirs: A case study, Nubia Sandstone Reservoir, Gulf of Suez, Egypt. Natural Resources Research, 28, 1587-1608

Elgendy, N.T.H., Abuamarah, B.A., Nabawy, B.S., Ghrefat, H., Kassem, O.M.K., 2020. Pore Fabric Anisotropy of the Cambrian–Ordovician Nubia Sandstone in the Onshore Gulf of Suez, Egypt: A Surface Outcrop Analog. Natural Resources Research, 29, 1307-1328.

Farag, I.A.M., 1959. Contribution to the study of the Jurassic Formation in the Maghara massif, N. Sinai. J. Geol. Soc. Egypt. 3, 175-195.

Gomaa, M.M., Kassab, K.A., El-Sayed, N.A., 2015. Study of pertrographical and electrical properties of some Jurassic carbonate rocks, north Sinai, Egypt. Egyptian Journal of Petroleum, 24 (3), 343-352.

Jenkins, D., 1990. Mesozoic sediments of Gebel El-Maghara, Northern Sinai. In: Said R (ed.). The geology of Egypt. Balkema, the Netherlands.

Jenkins, D., Harms, J., Oesleby, T., 1982. Mesozoic Sediments of Gebel Maghara, North Sinai, Arab Republic of Egypt. 6th Exploration Seminar, EGPC, Cairo, 1, 130-158.

Kassab, M.A., Abuseda, H.A., El Sayed, N.A., Lala, A.M., Elnaggar, O.M., 2016. Petrographical and petrophysical integrated studies, Jurassic rock samples, North Sinai, Egypt. Arabian Journal of Geosciences, 9, Article 99.

Kassab, M.A.M., Abu Hashish, M., Nabawy, B.S., El-Nagar, O., 2017. Effect of kaolinite as a key factor controlling the petrophysical properties of the Nubia sandstone in central Eastern Desert, Egypt. Journal of African Earth Sciences, 125, 103-117.

Kostandi, A.B., 1959. Facies maps for the study of the Paleozoic & Mesozoic sedimentary basins in the Egyptian Region, U.A.R, 1st Arab Petroleum Congress, 2, 33-51.

Martin, A.J., Solomon, S.T., Hartmann, D.J., 1997. Characterization of petrophysical flow units in carbonate reservoirs. AAPG. Bull., 81, 734-759.

Moustafa, A.P., Khalil, M., 1990. Structural characteristics and tectonic evolution of Northern Sinai fold belts, Egypt. In: R. Said (Ed.). The Geology of Egypt, 381-389.

Nabawy, B.S., 2018. Impacts of fossil anisotropy on the electric and permeability anisotropy of highly fossiliferous limestone: a case study. Marine Geophysical Research, 39(4), 537–550.

Nabawy, B.S., ElHariri, T.Y.M., 2008. Electric fabric of Cretaceous clastic rocks in Abu Gharadig basin, Western Desert, Egypt. Journal of African Earth Sciences, 52 (1-2), 55-61.

Nabawy, B.S., El Sharawy, M.S., 2015. Hydrocarbon potential, structural setting and depositional environments of Hammam Faraun Member of the Belayim Formation, Southern Gulf of Suez, Egypt. Journal of African Earth Sciences, 112, 93-110.

Nabawy, B.S., Wassif, N.A., 2017. Effect of the mineralogical composition on the petrophysical behavior of the amygdaloidal and vesicular basalt of Wadi Wizr, Eastern Desert, Egypt. Journal of African Earth Sciences, 134, 613-625.

Nabawy, B.S., El Sharawy, M.S., 2018. Reservoir assessment and quality discrimination of Kareem Formation using integrated petrophysical data, Southern Gulf of Suez, Egypt. Marine and Petroleum Geology, 93, 230-246.

Nabawy, B.S., Abd El Aal, A., 2019a. Effects of diagenesis on the geomechanical and petrophysical aspects of the Jurassic Bir El-Maghara and Masajid carbonates in Gebel El-Maghara, North Sinai, Egypt. Bulletin of Engineering Geology and the Environment 78 (7), 5409-5429

Nabawy, B.S., Abd El Aal, A., 2019b. Impacts of the petrophysical and diagenetic aspects on the geomechanical properties of the dolomitic sequence of Gebel El-Halal, Sinai, Egypt. Bulletin of Engineering Geology and the Environment 78 (4), 2627-2640.

Nabawy, B.S., Basal, A.M.K., Sarhan, M.A.,Safa, M.G., 2018. Reservoir zonation, rock typing and compartmentalization of the Tortonian-Serravallian sequence, Temsah Gas Field, offshore Nile Delta, Egypt. Marine and Petroleum Geology, 92, 609-631.

Nabawy, B.S., Elgendy, N.T.H., Gazia, M.T., 2019. Mineralogic and diagenetic controls on reservoir quality of paleozoic sandstones, Gebel el-zeit, north Eastern Desert, Egypt. Natural Resources Research, 29, 1215–1238.

Nabawy, B.S., Mansour, A.S., Rashed, M.A., Afify, W.S.M., 2020. Implementation of sedimentary facies and diagenesis on the reservoir quality of the Aquitanian-Burdigalian Rudeis Formation in the Gulf of Suez, Egypt: A comparative surface and subsurface study. Geological Journal, 55 (6), 4543-4563

Orodu, O.D., Tang, Z. Fei, Q., 2009. Hydraulic (Flow) Unit Determination and Permeability Prediction: A Case Study of Block Shen-95, Liaohe Oilfield, North-East China. Journal of Applied Sciences, 9, 1801-1816.

Shenawi, S.H., White, J.P., Elrafie, E.A., El-Kilany, K.A., 2007. Permeability and water saturation distribution by lithologic facies and hydraulic units: A reservoir simulation case study: 15th SPE Middle East Oil and Gas Show and Conference, Manama, Bahrain, March 11-14, SPE-105273-MS, 7.

Teh, W.J., Willhite, G.P., Doveton, J.H., 2012. Improved reservoir characterization using petrophysical xlassifiers within electrofacies. SPE-154341-PP.

Ti, G., Ogbe, D.O., Munly, W., Hatzignatiou, D.G., 1995. Use of flow units as a tool for reservoir description: A case study. SPE Format. Evaluation, 10, 122-128.

Tiab, D., Donaldson, E.C., 1996. Petrophysics, theory and practice of measuring reservoir rock and fluid transport properties (205-220). Houston, TX: Gulf Publishing Co.

Yussef, M.H.M., 1986. Sedimentological, biostratigraphical and geochemical studies of the Jurassic rocks in Gebel El Maghara area, North Sinai, Cairo Univ. Ph.D.

Zaki, R.M., 1996. Petrology and Geochemistry of the coal bearing Jurassic sediments, El-Maghara Area, Northern Sinai, Egypt. Ph.D., Thesis, Fac. Sci., Minia Univ., Egypt.

Figures

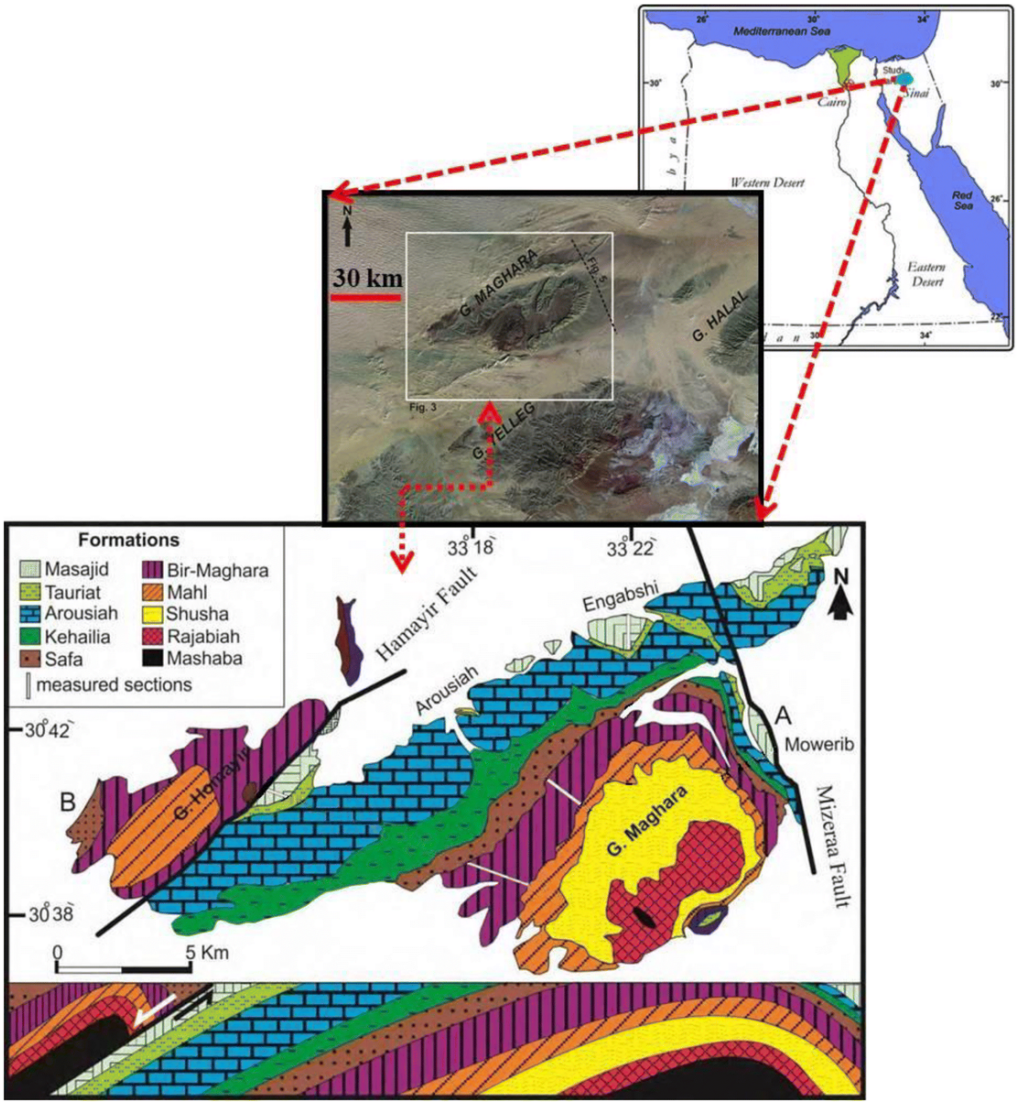

Figure 1

Location map, Landsat Thematic Mapper image, and geologic map of the Jurassic Gebel El-Maghara surface outcrop at its type section in north Sinai, Egypt, and a geologic cross-section of in Gebel El-Maghara mass (Nabawy and Abd El Aal, 2019a).

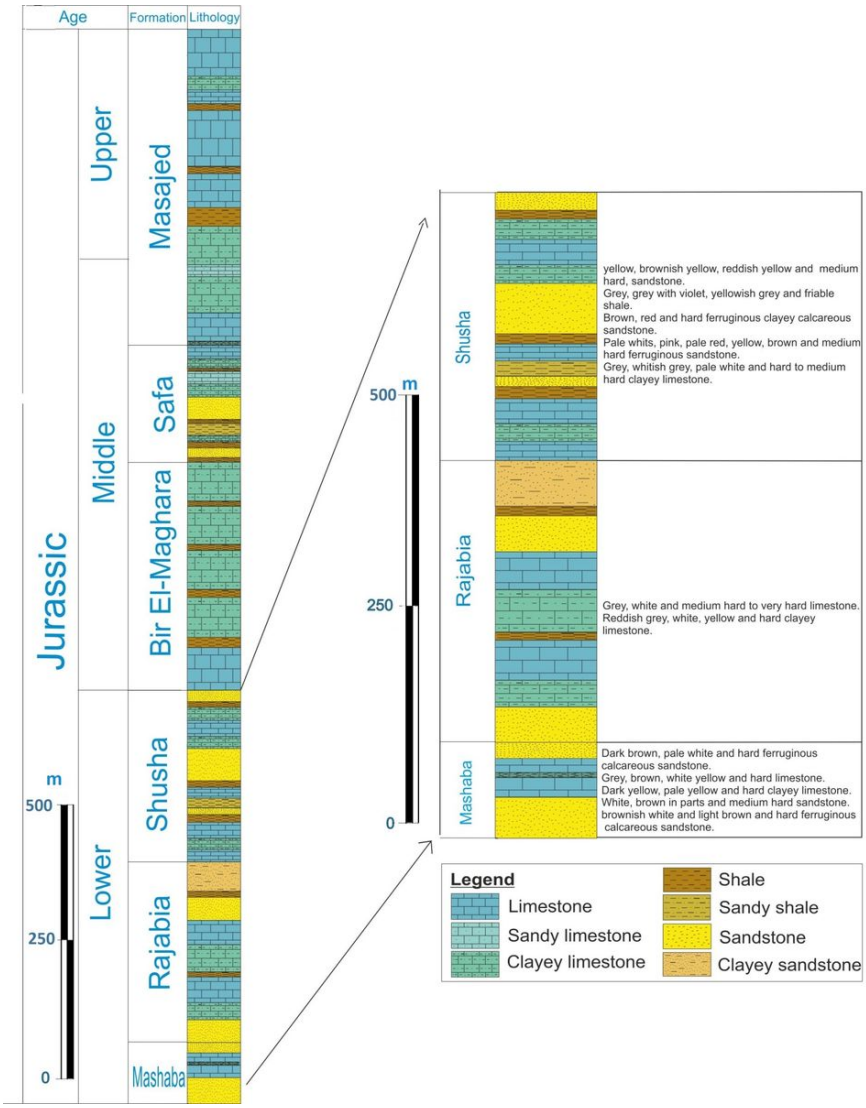

Figure 2

Lithostratigraphic section of Gebel El-Maghara (modified after Gomaa et al., 2015; Kassab et al., 2016).

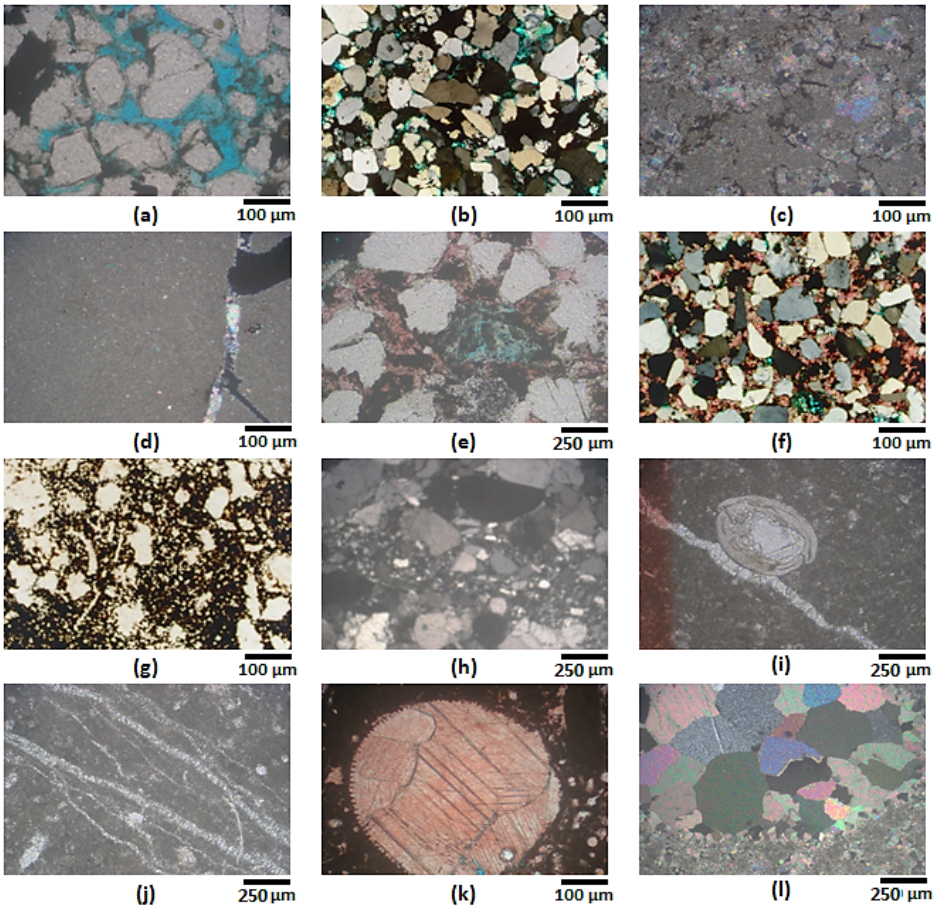

Figure 3

Photomicrographs of: (a) Siliceous quartz arenite microfacies, Rajabia Formation, MFA1, PPL, (b) Ferruginous kaolinitic siliceous quartz arenite, Rajabia Formation, MFA1, C.N., (c) Ferruginous dolomitic packstone, Shusha Formation, C.N., MFA1, (d) Ferruginous dolomitic packstone, Rajabia Formation, C.N., MFA1, (e) Ferruginous kaolinitic and sparitic quartz arenite, Shusha Formation, MFA2, C.N., (f) Highly ferruginous and sparitic quartz arenite, Shusha Formation, MFA3, C.N., (g) Highly ferruginous and sparitic quartz arenite, Rajabia Formation, MFA3, PPL, (h) Highly compacted siliceous lithic arenite, Mashaba Formation, PPL, MFA3, PPL, (i, j) Highly fractured bioclastic wackestone, Mashaba Formation, MFA3, PPL, and (k, l) Fractured bioclastic packstone microfacies, Mashaba Formation, MFA3, C.N.

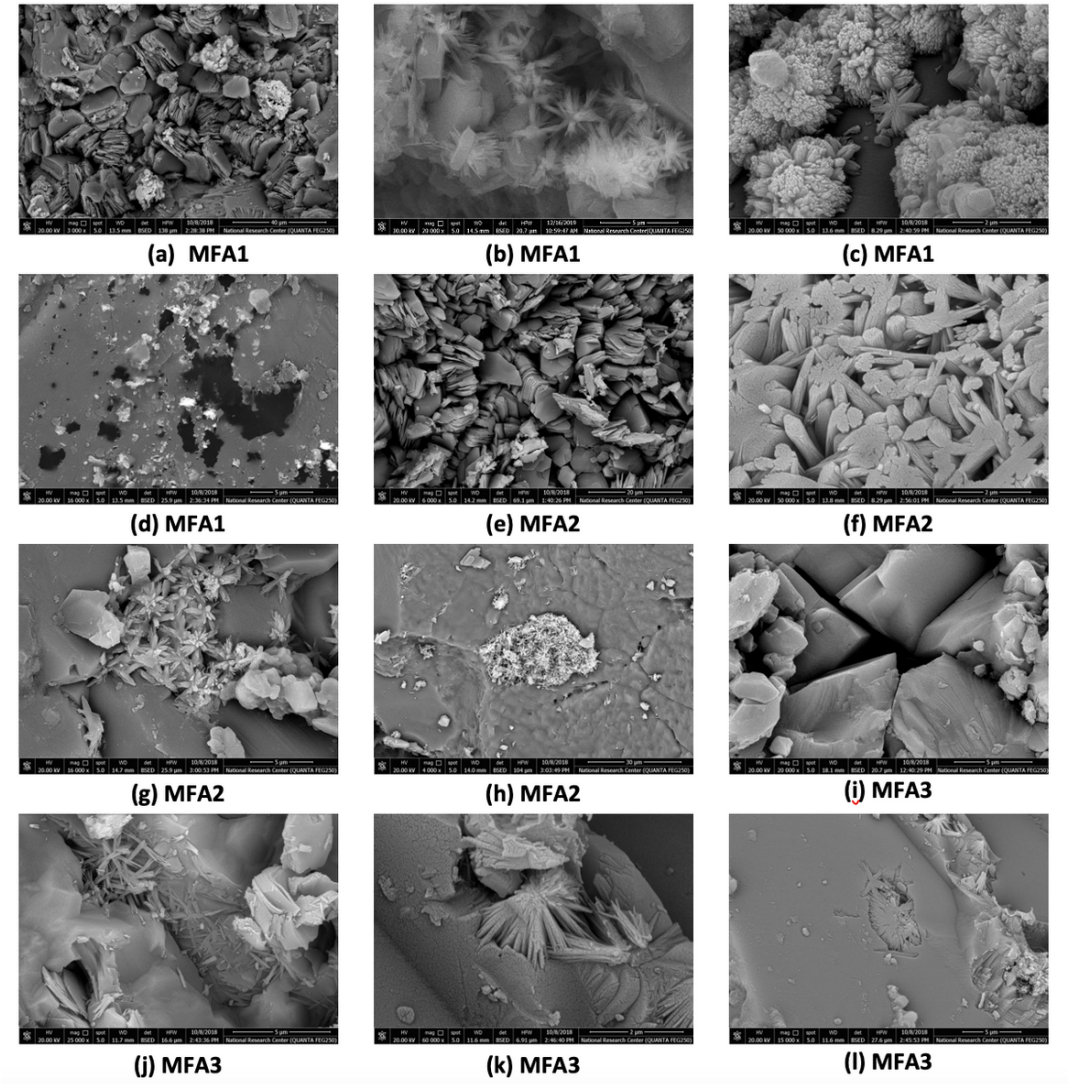

Figure 4

SEM images showing, (a, b, c) Ferruginous kaolinitic siliceous quartz arenite microfacies, Rajabia Formation, MFA1, (d) Ferruginous dolomitic packstone, Shusha Formation, MFA1, (e, f, g, h) Ferruginous kaolinitic and sparitic quartz arenite, Shusha Formation, MFA2, (i) Highly compacted siliceous lithic arenite, Mashaba Formation, MFA3, (j, k, l) Highly ferruginous and sparitic quartz arenite, Shusha Formation, MFA3.

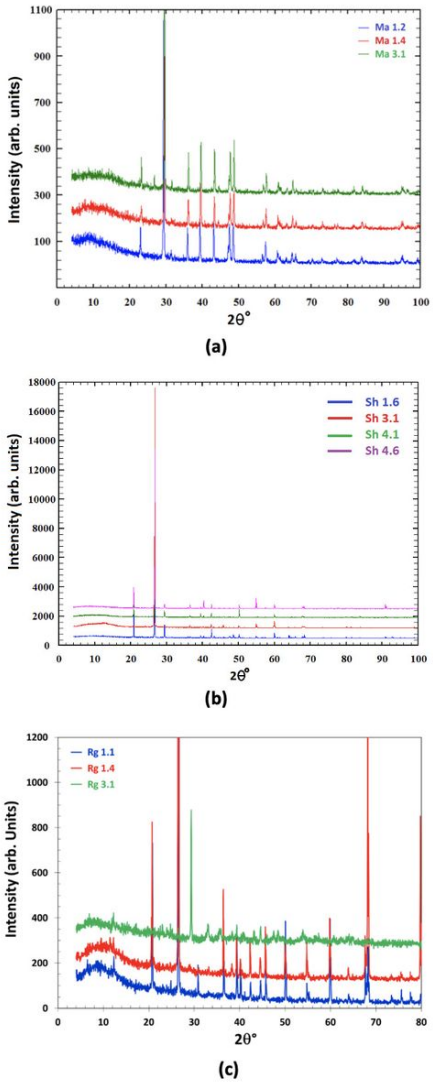

Figure 5

XRD analysis of the studied Lower Jurassic microfacies in Gebel El-Maghara area: (a) Mashaba Formation, (b) Shusha Formation, and (c) Rajabia Formation.

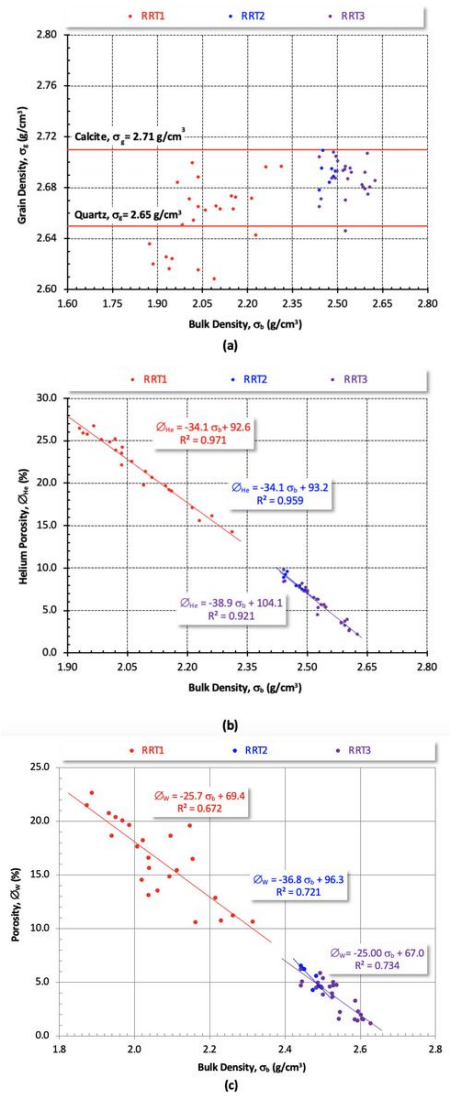

Figure 6

Plotting the bulk density (σb) versus: a) grain density (σg), b) helium porosity, and c) water porosity for the lower Jurassic samples.

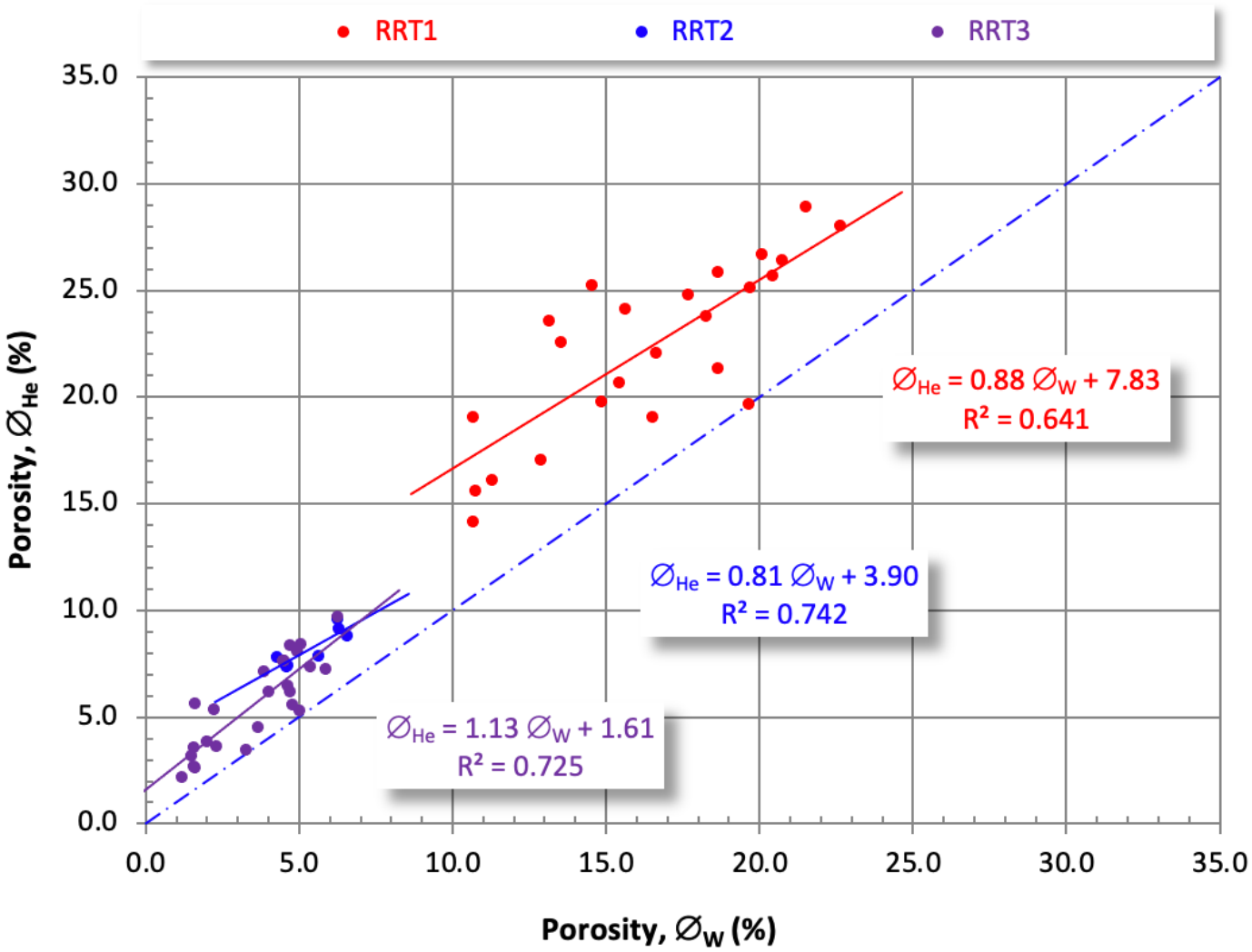

Figure 7

A correlation between the helium and water porosity of the studied samples.

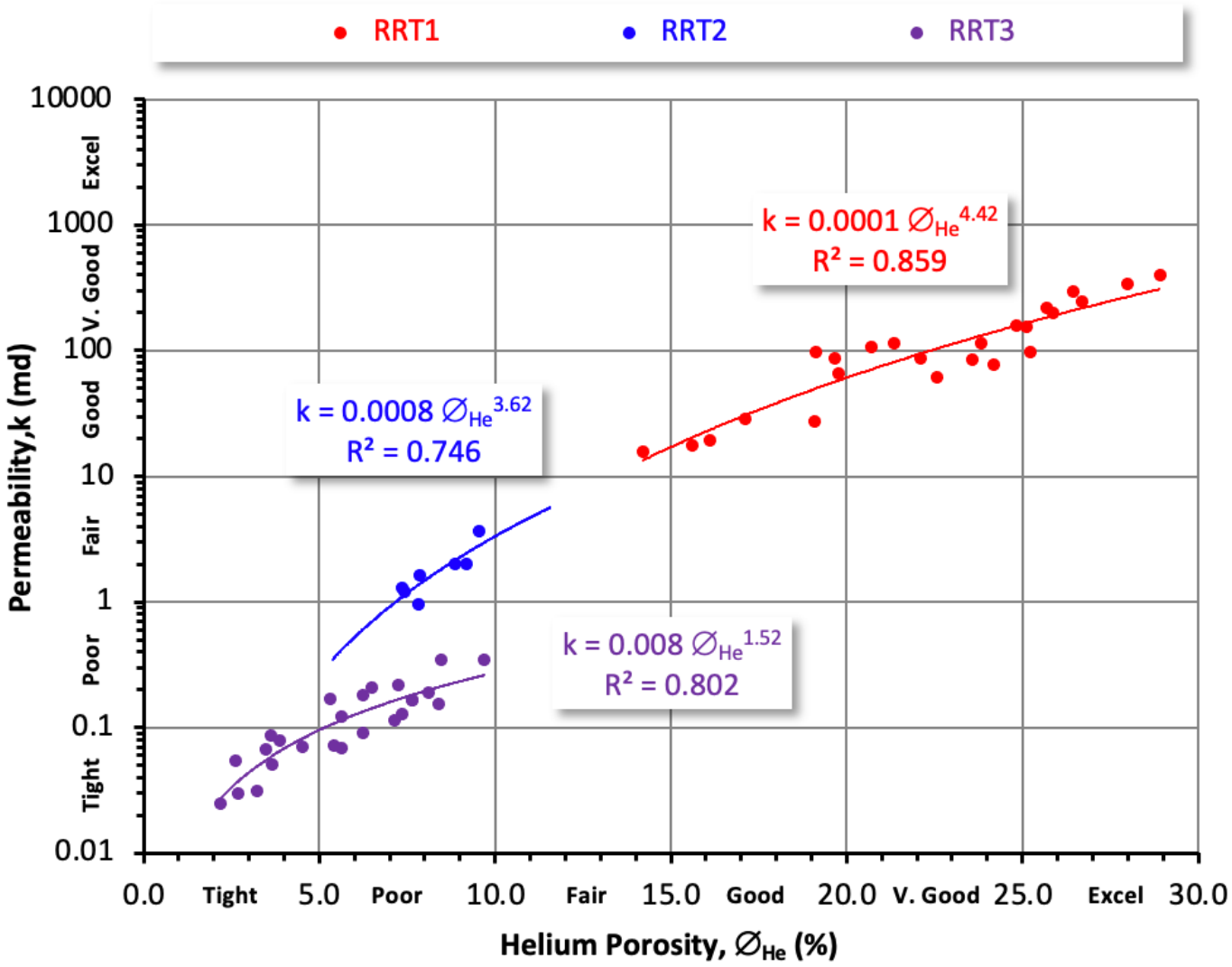

Figure 8

A correlation between the helium and water porosity of the studied samples.

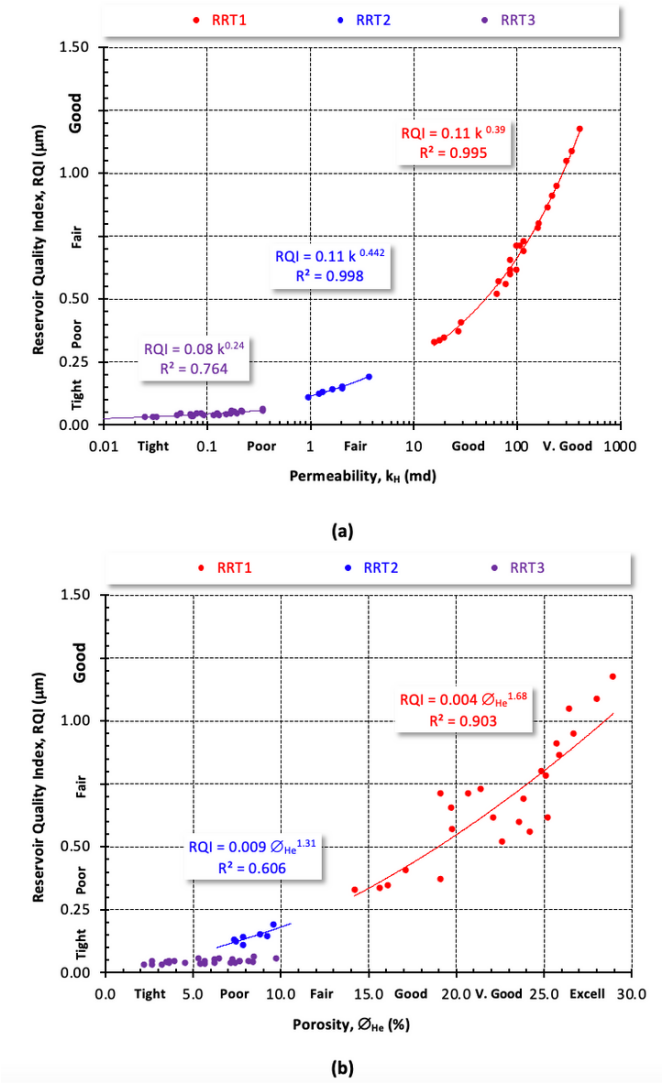

Figure 9

Plotting the reservoir quality index (RQI) as a function of: a) Permeability (k), and b) porosity (∅He) of the Lower Jurassic reservoir rock types (RRTs). The mentioned RQI, k, and ∅ classification ranks are following Nabawy et al. (2018).

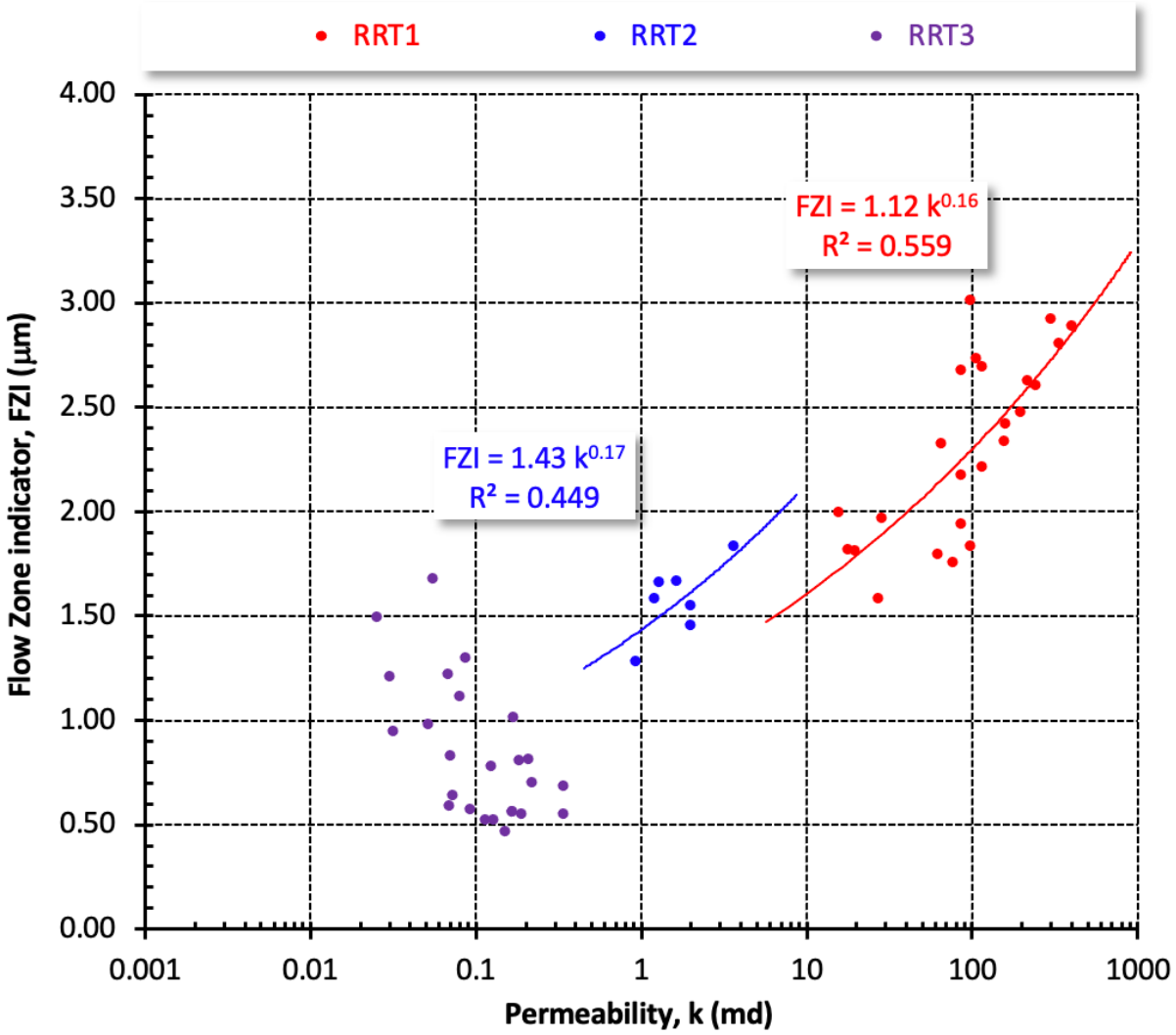

Figure 10

Plotting the flow zone indicator (FZI) as a function of Permeability for the Lower Jurassic samples.

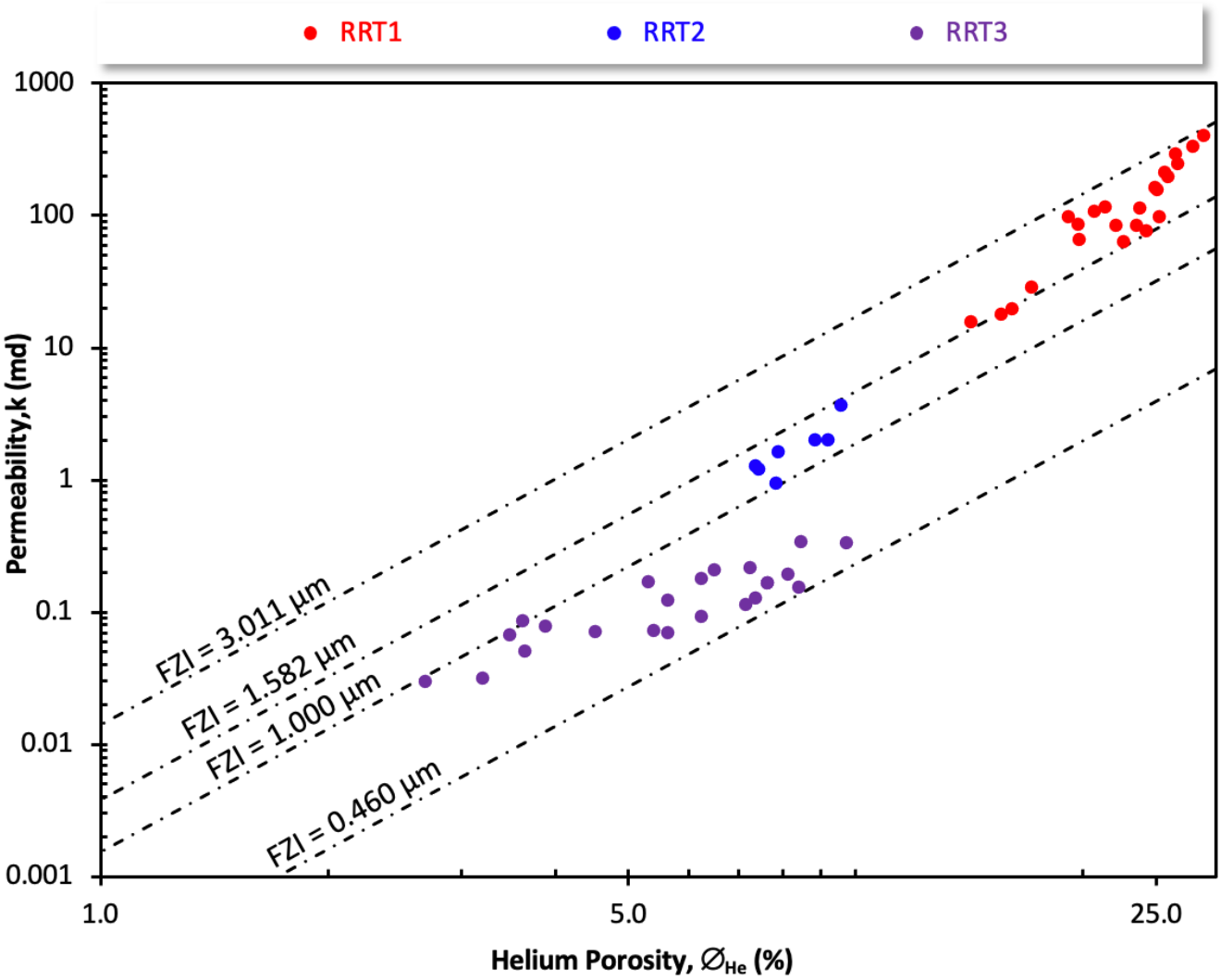

Figure 11

Reservoir rock typing based on the porosity-permeability plot superimposed with intersecting FZI lines.

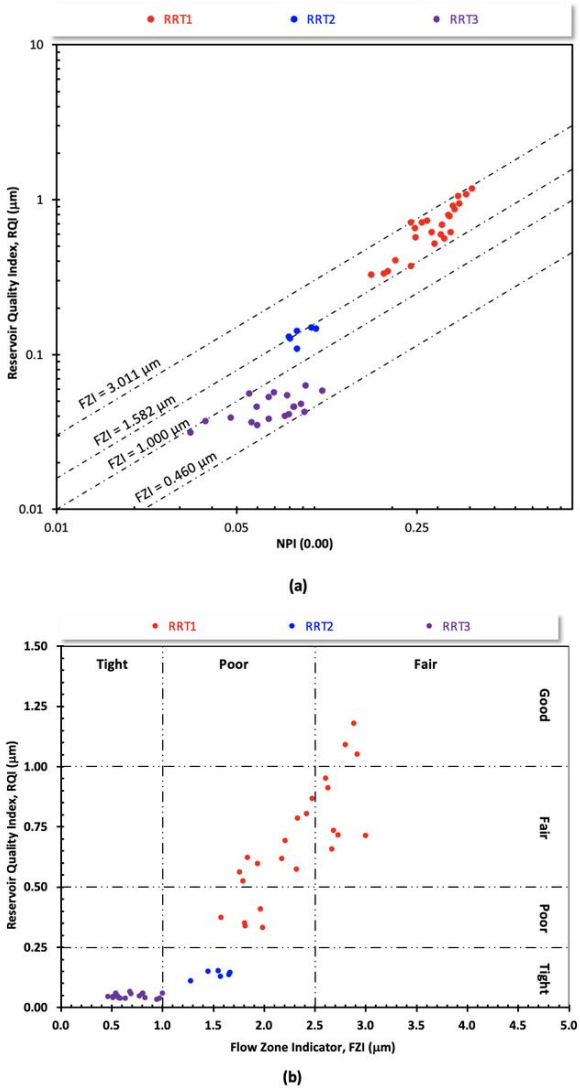

Figure 12

Reservoir quality assessment for the studied rock properties based on the reservoir quality parameters: (b) plotting the RQI versus FZI. The RQI and FZI values are based on the ranking values that proposed by Nabawy and ElHariri (2008), Nabawy et al. (2018).

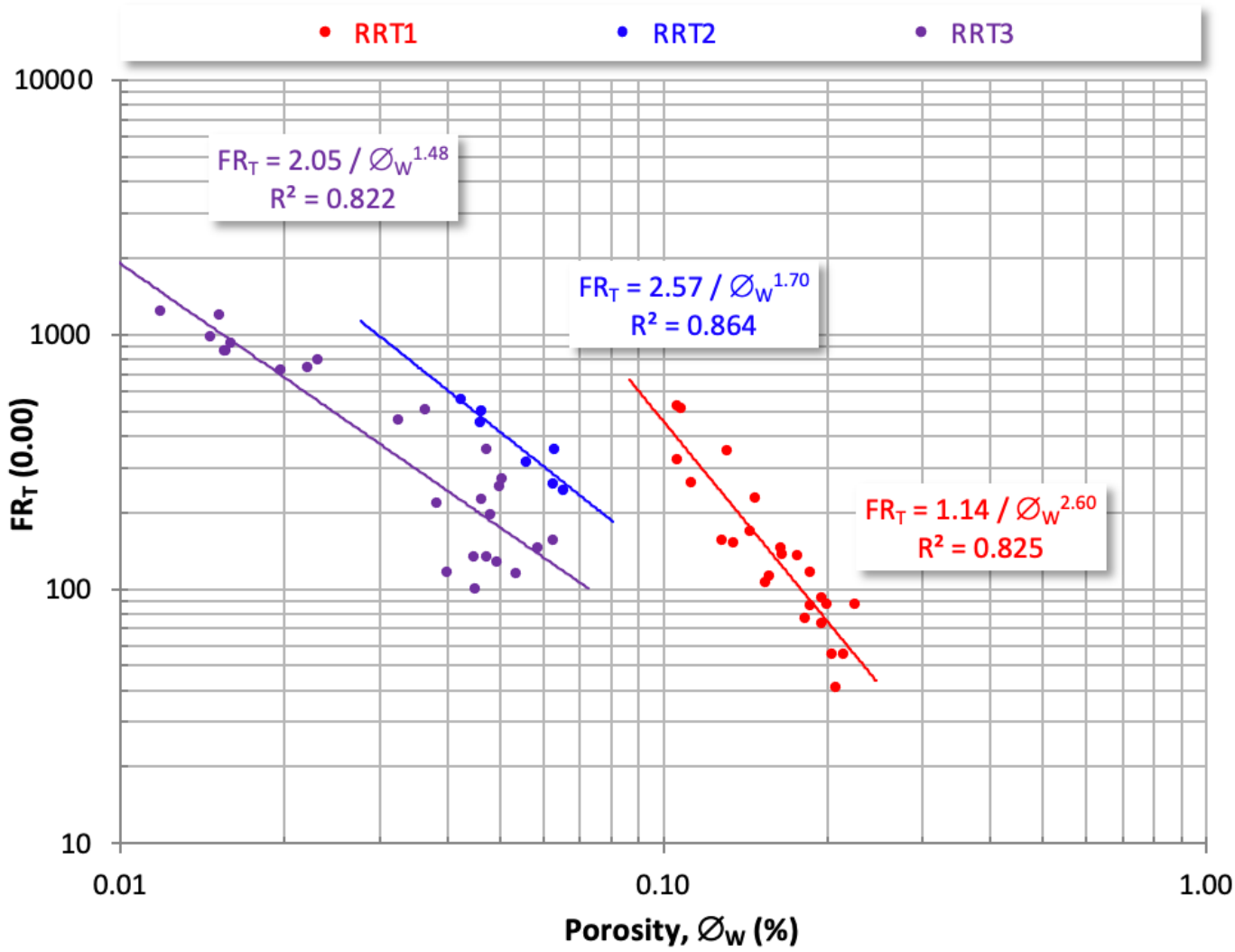

Figure 13

Archie's parameters determination based on the true formation resistivity- porosity plot (FRT-∅W).

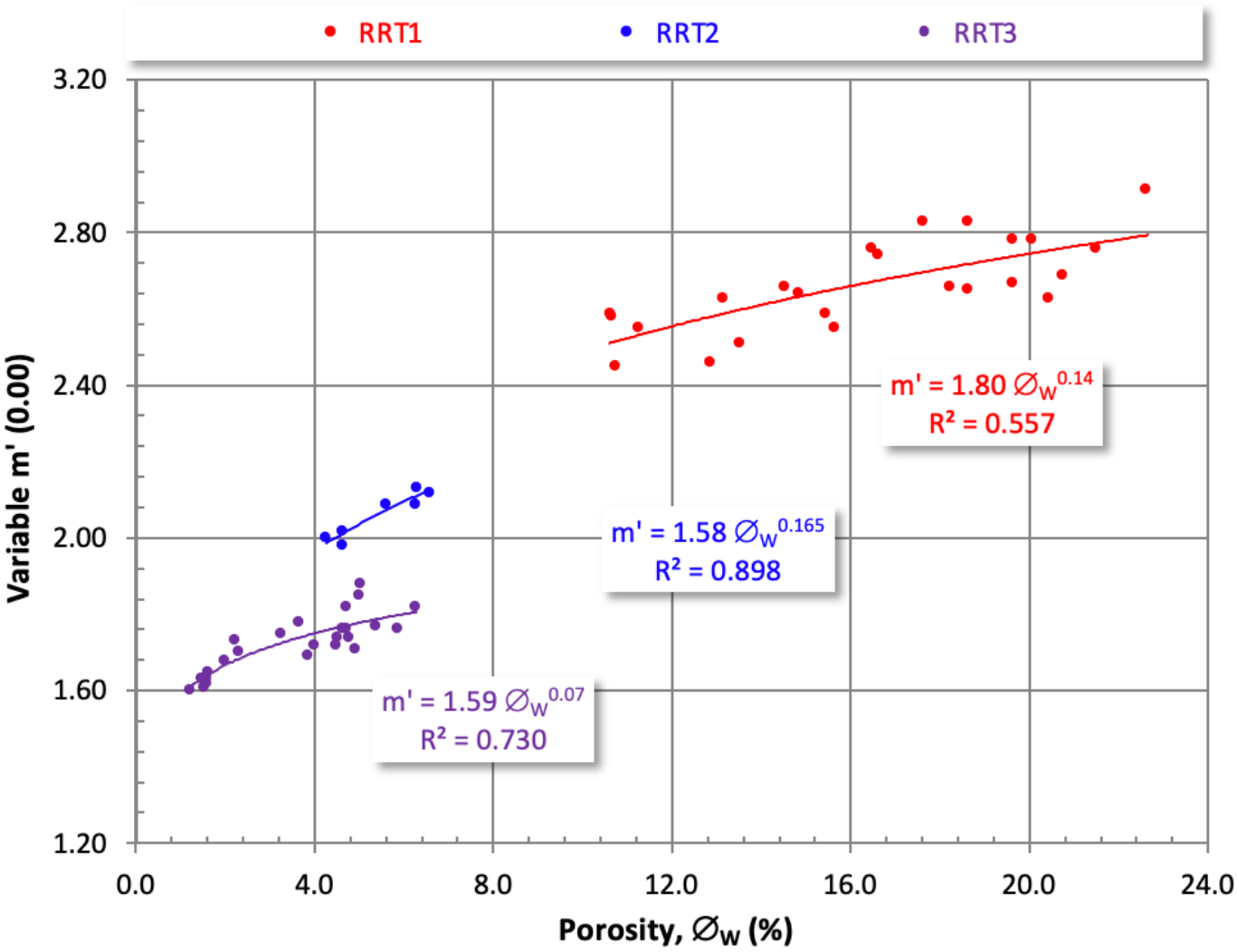

Figure 14

Plotting the variable porosity exponent (m') as a function of porosity measured by water injection.

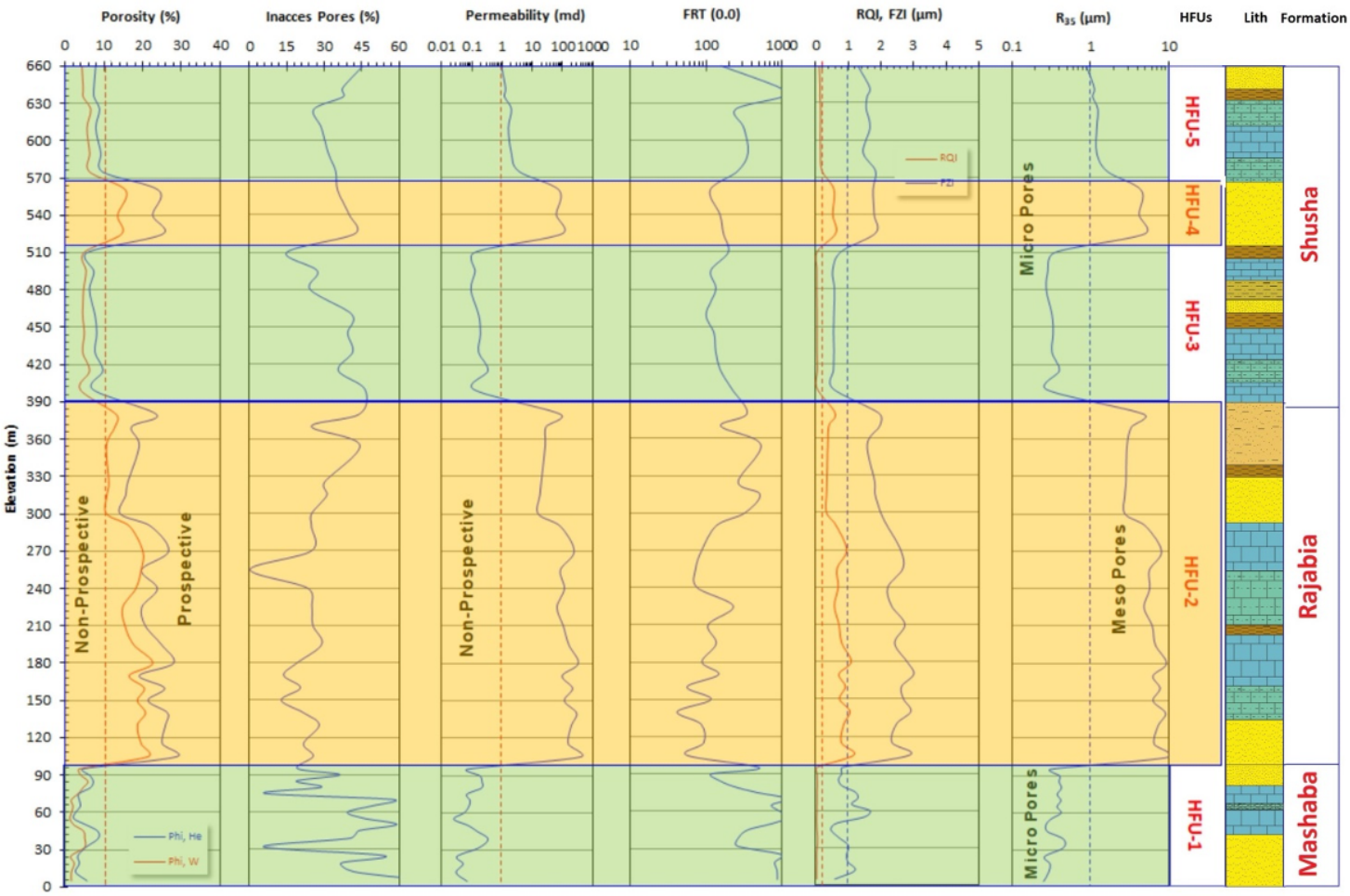

Figure 15

A vertical presentation for the petrophysical and reservoir quality parameters of the Lower Jurassic sequence in Gebel El Maghara area. Dashed lines refers to the applied cutoff values to differentiate between what is called prospective and non-prospective values for porosity ($\emptyset \geq 10$ %), permeability ($k \geq 1.0$ md), reservoir quality index (RQI ≥ 0.25 µm), flow zone indicator (FZI ≥ 1.0 µm), and R35 (1.0 µm $\leq$ R35). The sequence is classified into four hydraulic flow units (HFUs).

Supplementary Files

This is a list of supplementary files associated with this preprint. Click to download.

- Highlights.docx